

# A Stellar Magnesium to Silicon ratio in the atmosphere of an exoplanet

Jorge A. Sanchez<sup>\*1</sup>, Peter C. B. Smith<sup>1</sup>, Krishna Kanumalla<sup>1</sup>, Luis Welbanks<sup>1</sup>, Michael R. Line<sup>††1</sup>, Stefan Pelletier<sup>2</sup>, Steven Desch<sup>1</sup>, Patrick Young<sup>1</sup>, Jennifer Patience<sup>1</sup>, Jacob Bean<sup>3</sup>, Matteo Brogi<sup>4,5</sup>, Dan Jaffe<sup>6</sup>, Gregory N. Mace<sup>6</sup>, Megan Weiner Mansfield<sup>7</sup>, Vatsal Panwar<sup>8,9</sup>, Vivien Parmentier<sup>10</sup>, Lorenzo Pino<sup>11</sup>, Arjun Baliga Savel<sup>7</sup>, Lennart van Sluijs<sup>12</sup>, Joost P. Wardenier<sup>13</sup>

<sup>1</sup>*School of Earth and Space Exploration, Arizona State University, Tempe, AZ, USA*

<sup>2</sup>*Observatoire astronomique de l'Université de Genève, Switzerland*

<sup>3</sup>*Department of Astronomy and Astrophysics, University of Chicago, Chicago, IL, USA*

<sup>4</sup>*Dipartimento di Fisica, Università degli Studi di Torino, Torino, Italy*

<sup>5</sup>*INAF – Osservatorio Astrofisico di Torino, 10025 Pino Torinese, Italy*

<sup>6</sup>*Department of Astronomy, The University of Texas at Austin, Austin, TX, USA*

<sup>7</sup>*Department of Astronomy, University of Maryland, College Park, MD, USA*

<sup>8</sup>*Department of Physics, University of Warwick, Coventry, UK*

<sup>9</sup>*Center for Exoplanets and Habitability, University of Warwick, Coventry, UK*

<sup>10</sup>*Laboratoire Lagrange, Observatoire de la Côte d'Azur, CNRS, Université Côte d'Azur, Nice, France*

<sup>11</sup>*INAF – Osservatorio Astrofisico di Arcetri, Florence, Italy*

<sup>12</sup>*Department of Astronomy, University of Michigan, Ann Arbor, MI, USA*

<sup>13</sup>*Trottier Institute for Research on Exoplanets (iREx), Université de Montréal, Montréal, QC, Canada*

**The elemental compositions of exoplanets encode information about their formation environments and internal structures. While volatile ratios such as carbon-to-oxygen (C/O) are used to trace formation location, the rock-forming elements—magnesium (Mg), silicon (Si), and iron (Fe)—govern interior mineralogy and are commonly assumed to reflect the host star's abundances. Yet this assumption remains largely untested. Ultra-hot Jupiters, gas-giant exoplanets with dayside temperatures above 3,000 K, provide rare access to refractory elements that remain gaseous. Here we present high-resolution thermal emission spectroscopy of the exoplanet WASP-189b ( $T_{\text{eq}} = 3354^{+27}_{-34}$  K) obtained with the Immersion Grating Infrared Spectrometer (IGRINS) on Gemini South. We detect neutral iron (Fe I), magnesium (Mg I), silicon (Si I), water (H<sub>2</sub>O), carbon monoxide (CO), and hydroxyl (OH) at signal-to-noise ratios exceeding 4, and retrieve their elemental abundances. We show that the Mg/Si, Fe/Mg, and Si/Fe ratios are consistent with stellar values, while the refractory-to-volatile ratio is enhanced by roughly a factor of 2. These findings demonstrate that giant-planet atmospheres can preserve stellar-like rock-forming ratios, providing an empirical validation of the stellar-proxy assumption that underpins planetary composition and formation models across exoplanet systems.**

<sup>\*</sup>Corresponding author: [jasanchez@asu.edu](mailto:jasanchez@asu.edu)

<sup>†</sup>Corresponding author; senior author / supervised the project: [mrline@asu.edu](mailto:mrline@asu.edu)

## Introduction

Measurements of the elemental composition of planets enable fundamental constraints on how planets form, migrate, and evolve<sup>1,2</sup>. Exoplanet atmospheres of giant planets, in particular, offer a unique window<sup>3</sup> into the processes occurring within proto-planetary disks that shape planetary systems, augmenting stellar and Solar-System material abundance measurements. Volatile (ices), elements such as carbon and oxygen have been extensively used to trace the origins and migration histories of giant planets<sup>4–7</sup>, revealing a wide diversity in potential formation scenarios<sup>8</sup> across the exoplanet population. However, these volatile diagnostics are strongly influenced by condensation fronts (ice-lines) and other disk chemical processes<sup>9</sup> limiting their utility in fully linking present-day atmospheric composition to the processes that sculpted their birth<sup>7</sup>.

Ref.'s<sup>10,11</sup> highlighted the utility of giant planet atmosphere refractory elemental (e.g., Fe, Mg, Si) constraints as a tracer of the rocky material within protoplanetary disks. Because these elements condense at high temperatures, their relative abundances are expected to remain nearly constant throughout the disk<sup>11,12</sup>, providing a compositional baseline that links stars, giant planets, and terrestrial bodies. Measurements of volatile-to-refractory enrichments in ultra-hot Jupiters (UHJs)—where both volatile and refractory species persist in the gas phase within the atmosphere—have begun to reveal how rocks and ices are incorporated into planetary envelopes<sup>10,11,13,14</sup>. Furthermore, the same rock-forming ratios (Mg/Si and Fe/Mg) govern the mineralogy, core size, and mantle rheology of terrestrial planets<sup>15–17</sup>. For these worlds, direct elemental composition measurements are not yet possible; hence, modeling investigations of terrestrial exoplanets inherently assume that the bulk planetary composition reflects that of the host star. Testing this assumption observationally by measuring refractory ratios in giant-planet atmospheres provides the necessary benchmark for interpreting the composition of rocky and giant planets alike.

Here we show, with high-resolution thermal emission spectroscopy of the ultra-hot Jupiter WASP-189b, direct constraints on both refractory (Mg, Si, Fe) and volatile (C, O) elemental ratios. We find that WASP-189b's atmospheric refractory elemental ratios reflect those of its host star, providing an empirical validation of the assumption of using stellar abundances as a proxy for refractory composition.

## Results

### Observations

We obtained high resolution ( $R$  approximately 45,000) thermal emission spectra of WASP-189b (planet radius,  $R_P = 1.6 \pm 0.017 R_{\text{Jup}}$ , planet mass,  $M_P = 1.99 \pm 0.16 M_{\text{Jup}}$ )<sup>18,19</sup> using IGRINS<sup>20</sup>,

formerly at Gemini South. Previous studies using IGRINS have detected individual volatile species ( $\text{H}_2\text{O}$ ,  $\text{CO}$ ,  $\text{OH}$  <sup>21,22</sup>) and the combination of multiple refractory species ( $\text{Fe I}$ ,  $\text{Mg I}$ ,  $\text{Si I}$ ,  $\text{Ti I}$ ,  $\text{Ca I}$ ,  $\text{Cr I}$ ,  $\text{V I}$ , <sup>14</sup>) in the atmospheres of giant planets, due to the instruments broad and near continuous wavelength coverage ( $1.4 - 2.5 \mu\text{m}$ ) over which many of these species have spectral features (Figure 1, panel b). Observations of WASP-189b were conducted over two separate nights (2022-05-07 and 2023-04-02 UTC), taken just prior to (night 1) and following (night 2) secondary eclipse, capturing the thermal emission of the planet’s day-side hemisphere. Supplementary Figure 1 shows the median SNR and humidity during the night for each observation. Over the course of each observation, dozens of individual spectra are taken at different phases in the planetary orbit (Figure 1, panel a). To isolate the faint planetary signal from Earth’s telluric lines and the stellar features in each of our spectra, we apply standard detrending procedures following <sup>21,23,24</sup> (see Methods, subsection Observations and Data Reduction). The detrending process removes these dominant features, while preserving the planet signal within the residual data.

## Gas Detections

We generate a model spectrum (labeled Fiducial Model in Figure 2), meant to match the thermal emission signal from the planet to compare with our post-detrended data. During our observations, the spectral lines of the planet are constantly Doppler-shifted by the planet’s orbital motion. We therefore also shift the generated model spectrum along a range of line of sight velocities, and calculate a cross-correlation coefficient between the data and shifted model <sup>14,25</sup> (see Methods, subsection Gas Detection via Cross-Correlation). The peak value of the cross-correlation coefficient (CCF), will occur at the velocity shifts that best match the model with the observed data for that orbital phase. Repeating this process in time with all spectra taken throughout the night reveals a coherent trail in velocity-phase space that traces the planet’s motion <sup>21,23</sup>. Figure 2 shows this trail for three model configurations: The first is our fiducial model (Figure 2, panel a), which is a combination of both volatile ( $\text{H}_2\text{O}$ ,  $\text{CO}$ ,  $\text{OH}$ ) and refractory gases ( $\text{Fe I}$ ,  $\text{Mg I}$ ,  $\text{Si I}$ ,  $\text{Ti I}$ ,  $\text{Ca I}$ ,  $\text{V I}$ ). We included these gases in our fiducial model due to their previous detections on other ultra-hot Jupiters <sup>22,26,27</sup>, and their expected volume mixing ratios of  $> 10^{-5}$  based on the theoretical gas abundance profiles for WASP-189b in shown panel c of Figure 1. Panels b and c of Figure 2 isolate the contribution of the volatile and refractory gases, using models containing each set of species separately. The clear presence of trails in all three configurations indicates that multiple species from both volatile and refractory groups are present in WASP-189b’s dayside atmosphere.

To detect the signature of individual molecular and atomic species in the observed spectrum, we sum the correlation coefficient along the orbital path taken by the planet during our observations. By calculating this summed correlation coefficient as a function of different velocities (Keplerian velocity  $K_p$ , and an offset from the star-planet system velocity  $dV_{\text{sys}}$  in Figure 3), we isolate the total atmospheric signal for a given single model template. A species is considered strongly detected if the peak signal—which should near the expected  $K_p$  and  $dV_{\text{sys}}$  pair—is detected

at a signal-to-noise ratio of at least 4 relative to the background <sup>21</sup> (see Methods, subsection Gas Detection via Cross-correlation). Figure 3 summarizes the detections of individual gases. We find strong detections of both refractory and volatile species: Fe I ( $8.51\sigma$ ), CO ( $6.22\sigma$ ), Si I ( $5.91\sigma$ ), OH ( $5.79\sigma$ ), Mg I ( $4.71\sigma$ ) and H<sub>2</sub>O ( $4.36\sigma$ ).

## Elemental Abundance Determinations

To obtain quantitative estimates on the atmospheric elemental abundances, we employ Bayesian inference methods for parameter estimation, also known as retrievals <sup>21,22,28,29</sup>. Our framework couples an atmospheric model <sup>21,22,25</sup> with the affine-invariant ensemble Markov-chain Monte Carlo sampler <sup>30</sup>, to obtain constraints on elemental abundances, vertical temperature structure, and the Keplerian/system velocities. The atmospheric forward model assumes <sup>13,31</sup> thermochemical equilibrium <sup>32</sup> for the molecular and atomic gases in WASP-189b given the elemental abundance ratios and the temperature-pressure profile. This parameterization is preferred for ultra-hot Jupiters as the high temperatures result in kinetic timescales that are short compared to disequilibrium processes (photochemistry, transport) timescales, resulting in equilibrium gas abundances throughout the atmosphere <sup>33–35</sup>. The elemental abundance parameters are of the form

$$[X/Y]_{\odot/*} = \log_{10} \left( \frac{(X/Y)}{(X/Y)_{\odot/*}} \right). \quad (1)$$

where  $[X/Y]_{\odot/*}$  denotes  $\log_{10}$  of species X relative to Y, relative to X/Y in the sun ( $\odot$ ) <sup>36</sup>/star (\*). Our model also includes a parameterized temperature-pressure profile prescription similar to one described in <sup>14</sup>(see Methods, subsection Atmospheric Modeling and Retrieval Frameworks). All the parameters included in the model are listed with their sampled prior ranges in Table 1.

The resultant parameter constraints are summarized in Supplementary Data Figure 3. We compare the retrieved elemental abundances found in WASP-189b with those measured in the host star from <sup>18</sup>. These results are summarized in panel a of Figure 4. The retrieved refractory abundances are consistent to within approximately  $1\sigma$  to those measured in the star from ref <sup>18</sup>, while the C and O abundances are slightly sub-stellar (consistent within  $2\sigma$ ). We also compare our retrieved planet-to-star abundance ratios with other sets of stellar abundances of the host star found in the literature, summarized in Supplementary Table 1. Given the high temperatures of the atmosphere by WASP-189b, we note that we do not expect the depletion of any elemental abundances due to night-side cold-trapping <sup>37</sup> (see Supplementary Figure 6). Additionally, while many chemical species are expected to ionize at low pressures in UHJs <sup>37,38</sup>, our use of a chemical equilibrium prescription for the atmosphere accounts for these processes. We therefore do not expect either process to impact our final abundance calculations.

From the retrieved elemental abundances, we compute  $[\text{Mg}/\text{Si}]_* = -0.18^{+0.20}_{-0.21}$ ,  $[\text{Mg}/\text{Fe}]_* = 0.05^{+0.22}_{-0.22}$  and  $[\text{Si}/\text{Fe}]_* = 0.24^{+0.18}_{-0.18}$ . In line with expectations from similar analyses on other UHJs<sup>13,14,37,38</sup>, the Mg/Fe and Si/Fe ratios are consistent with their reported stellar values (here relative to ref<sup>18</sup>) at the 1 to 2  $\sigma$  confidence level. Our analysis also confirms this lack of divergence from the stellar composition for the Mg/Si ratio in WASP-189b, further supporting the assumption that all three species (Mg, Fe, Si) would remain in similar proportions to the stellar value within the disk<sup>12,39</sup>. Supplementary Figure 5 also shows the consistency of our derived Mg/Si ratio against different listed stellar abundances for WASP-189 found in the literature as well as comparisons with the solar value and local FGK stars Mg/Si ratio measurements.

We determine the total atmospheric metal (M—anything heavier than hydrogen, H, and helium, He, relative to H) enrichment and C/O ratio to be consistent with stellar values at the 68% confidence level ( $[\text{M}/\text{H}]_* = -0.25^{+0.33}_{-0.26}$ ,  $\text{C}/\text{O} = 0.49^{+0.10}_{-0.09}$ , the stellar C/O is 0.40<sup>18</sup>). We also measure a moderately super-stellar refractory ( $\text{R}=\text{Fe}+\text{Mg}+\text{Si}+\text{Ti}+\text{Ca}+\text{V}$ )-to-volatile ( $\text{V}=\text{C}+\text{O}$ ) ratio of  $[\text{R}/\text{V}]_* = 0.38^{+0.18}_{-0.19}$  ( $2.42^{+1.21}_{-0.87} \times$  the stellar value), and a refractory content  $[\text{R}/\text{H}]_*$  of  $0.01^{+0.36}_{-0.29} \times$  the stellar value. (See Supplementary Discussion). This composition is broadly consistent with formation interior to the snow lines of the disk, but the uncertainties on our measurements cannot rule out formation beyond the CO snow line (Supplementary Figure 7). We also emphasize the consistency of Mg, Si, and Fe with stellar values indicates that these elements behave interchangeably as refractory species, as theoretically predicted<sup>10,11</sup>. Consequently, constraining any one of these species may suffice to estimate a planet’s refractory enrichment and R/V (provided that species is not subject to condensation), simplifying future observational programs aimed at characterizing the volatile-to-refractory ratio.

## Discussion

As there are no other exoplanets with measured Mg/Si ratios, we weigh our results against other astrophysical objects with this measurement in Figure 4. These include the Earth and Sun, CI carbonaceous and enstatite chondrites, local FGK stars (green)<sup>40</sup>, and a subset of polluted white dwarfs (yellow)<sup>41</sup>. The spectra of polluted white-dwarfs are thought to encode the record of infalling planetary or cometary material post main-sequence<sup>42–44</sup>. However, the elemental abundances of the progenitor star remain unknown due to gravitational settling, making it impossible (unless they exist within a binary star system<sup>45</sup>) to link the planetary and stellar composition for those systems. The measurement of the Mg/Si ratio on WASP-189b (red) allows for the direct comparison of a planet’s Mg/Si ratio with not only its host star, but also with other objects having this measured quantity, showing consistency with many polluted WDs, along with the solar local FGK population. Our result expands the diversity of environments in which the Mg/Si ratio has been measured, extending this key geochemical metric from Solar System materials and disrupted planetary debris to the atmosphere of a gas giant exoplanet.

To explore the geochemical context of our measured abundance ratios, we calculate the relative proportions of Mg, Si, and Fe in WASP-189b’s atmosphere. Based on the retrieved abundances, we derive a Mg:Si:Fe ratio of approximately 1.2:1.0:0.7, which falls between the typical values found in enstatite and ordinary chondrites <sup>46</sup>. If a rocky planet were to form from material with this composition, its upper mantle would likely consist of a mixture of olivine and pyroxene, similar to Earth’s <sup>15,16</sup>. While we do not claim that giant planet atmospheres and rocky planet interiors evolve identically, both draw from the same disk reservoir of refractory solids <sup>12</sup>. The atmospheres of gas giants—particularly those with minimal condensation or cold-trapping (like WASP-189b, see supplementary material, section Thermal Structure)—are expected to retain the elemental ratios of the accreted refractory species, thereby serving as observable tracers of the disk’s bulk refractory composition <sup>10,11</sup>. The consistency of WASP-189b’s atmospheric Mg/Si, Mg/Fe, and Si/Fe ratios with the host star supports the assumption—widely used in terrestrial planet interior modeling <sup>15,16</sup>—that stellar refractory abundances trace the bulk composition of solids in the protoplanetary disk <sup>11,12,47,48</sup>. In this sense, measurements of these ratios in ultra-hot Jupiters offer an observational anchor for understanding the link between planet and host star composition, and ultimately the refractory building blocks in planetary systems.

By measuring the abundances of Si, Mg, and Fe in an exoplanet atmosphere, we show that the full set of rock-forming elemental ratios (Mg/Si, Mg/Fe, Si/Fe) exist in the same relative proportion as the host star, within measurement uncertainties. In doing so, we provide initial observational evidence that an Mg/Si ratio of an exoplanet matches that of its host-star, strengthening the stellar abundance ratio assumption used in interior models of rocky and volatile-rich exoplanets <sup>39,47</sup>. Along with measurements of volatile species such as carbon and oxygen, this multi-species analysis illustrates the wealth of information that can be gained from studying giant planets at high spectral resolution. Multi-wavelength, high-spectral resolution campaigns to study these kinds of systems both now and with the upcoming Extremely Large Telescope’s offer the opportunity to reveal the larger chemical inventory that exists within alien worlds. This effort will lead to even more precise measurements on the planet-star abundance patterns, for refined estimates on the chemical evolution and compositional diversity that exists within exoplanetary systems.

## Methods

### Observations and Data Reduction

Using the IGRINS instrument on (formerly on Gemini South <sup>20,49</sup>) we observed two separate half-nights of data capturing the direct thermal emission of the ultra-hot Jupiter WASP-189b. The first, taken on UTC 2022-05-07 as part of the Large and Long Program GS-2021-LP-206 (PI M. Line—The Roasting Marshmallows Survey), consisted of a 4.82 hour long continuous sequence of 28s exposures in an AB-BA nodding pattern while the planet was in the pre-secondary eclipse

phases ( $0.373 < \phi < 0.464$ ). This pre-eclipse sequence had a total of 155 AB pairs (hereafter referred to as frames). The second sequence was taken on UTC 2023-04-02 as part of the Queue program GS-2023-Q-23 (PI J. Sanchez) and consisted of a 3.23 hour long continuous sequence of 28s exposures resulting in 104 frames. 17 frames of this sequence were taken during secondary eclipse and were discarded. The final sequence considered here consisted of 84 frames covering orbital phases  $0.533 < \phi < 0.583$ . Median SNR's for each observation, as well as the humidity across the entire sequence for each night are shown in Supplementary Figure 1.

The raw data were calibrated and 1D spectra were extracted per frame by the IGRINS facility team using version 2 of the IGRINS Pipeline Package (PLP, <sup>49,50</sup>). We then used the publicly available `cubify` pipeline (<https://github.com/petercbsmith/cubify>) to process the PLP output into data cuboids of shape  $N_{\text{orders}} \times N_{\text{frames}} \times N_{\text{pixels}}$ , calculate the planet's orbital phase at each frame as well as the barycentric velocity of the observer for a given time of observation. `cubify` also applies a secondary wavelength realignment to each frame, discarding orders at the edge of the H and K band typically heavily contaminated by tellurics (with a median SNR being approximately  $< 200$ ), as has been done in previous analysis using IGRINS <sup>14,21,25,51</sup>. `cubify` can also perform a variety of detrending methods to data taken at high spectral resolution, including singular value decomposition, described in the following paragraph.

The dominant features of each spectrum are the quasi-stationary telluric and stellar lines as well as the wavelength-dependent instrument throughput. To detrend the data, we apply a singular value decomposition (SVD<sup>21,22,52</sup>) to each  $N_{\text{frames}} \times N_{\text{pixels}}$  data matrix per order. This process identifies the most representative features in the data (i.e., the most dominant modes) as the first number of right singular vectors in the matrix decomposition. The removal of these vectors from the data removes the contribution of these dominant modes. Left behind is relatively faint planet signal within the residual data matrix. To allow subsequent reproduction of the SVD effects on each tested model <sup>21,28,53</sup>, we recompose the data matrix using the same number right singular vectors originally removed to create a noiseless reconstruction of the raw data. For each night, we elect to remove the first six singular vectors, as this value is enough to remove visible telluric features in most of the IGRINS orders.

## Atmospheric Modeling and Retrieval Frameworks

The high spectral resolution model templates used both for the cross-correlation and retrieval analyses were calculated using a GPU-accelerated version of the exoplanet atmospheric forward modeling code CHIMERA <sup>21</sup>. CHIMERA takes as inputs the atmospheric temperature-pressure profile and the gas volume mixing ratio (VMR) profiles and outputs a high resolution ( $R=250,000$ ) thermal emission spectrum given the relevant absorption cross-sections/opacities.

The construction of the temperature-pressure grid utilized for our analysis is similar to the

one presented originally in <sup>14</sup>. Briefly, the shape of the profile is described by 6 pressure ‘nodes’, one at the bottom and top of the atmosphere and 4 additional points that can take on any pressure value between the prior ranges listed in Table 1. Each of the pressure nodes has an associated temperature, with prior ranges also listed in Table 1. These nodes define a set of ‘control points’ within the pressure-temperature space, and it is from these control points that our final grid of temperatures is calculated via the interpolation of these 6 temperature values onto a finer pressure grid using a Bézier Spline. This parametrization of our P-T profile allows for minimal assumptions to be made on its shape, providing flexibility on the lapse rate of the profile while also allowing for thermal inversions in the upper atmosphere, an expected feature of ultra-hot Jupiters due to the increased opacity of optical absorbers <sup>54,55</sup>.

To calculate pressure-dependent gas VMR profiles, we pass a given P-T profile and a vector of elemental abundances through the equilibrium chemistry code `FASTCHEM` <sup>56</sup>. `FASTCHEM` has routinely been used in the investigation of exoplanet and brown dwarf atmospheres, using instruments from both ground and space <sup>57–59</sup>.

We include the opacity of several species with spectral features in the H and K bands that are expected to be present at WASP-189 b’s temperatures. This includes the volatile bearing molecules H<sub>2</sub>O, CO, and OH as well as the following refractory species: Fe I, Mg I, Si I, Ti I, Ca I, V I. We also include the continuum opacity sources from H<sub>2</sub>-H<sub>2</sub> and H<sub>2</sub>-He collisional induced absorption as well as H<sup>-</sup> bound-free and H-e<sup>-</sup> free-free absorption. The sources of our opacity line-lists can be found in Supplementary Note 1. High resolution cross-sections are generated over a grid of temperatures and pressures covering several orders of magnitude in atmospheric pressure from 10<sup>2</sup> - 10<sup>-6</sup> bar and 2000 to 4000 Kelvin (temperatures past 4000K use the final value). Cross-sections for H<sub>2</sub>O, CO and OH are generated with the `HELIOS-K` tool <sup>60</sup> at 0.001 cm<sup>-1</sup> resolution and a line wing cutoff of 100 cm<sup>-1</sup> using the information provided in the exomol param files. Atomic cross-sections (over the same grid of pressure and temperature) are generated using a custom routine that considers both natural and pressure (via van-der Waals) broadening. Cross-sections are then interpolated (not averaged or binned) down to a constant R=250,000 for use within the `CHIMERA` radiative transfer routines.

The resultant planet thermal emission spectrum is converted to planet-star contrast by dividing the planet spectrum by a `PHOENIX` stellar model <sup>61</sup> (Teff = 8000 [K], logg = 4.06 [cgs], <sup>19</sup>) interpolated to the IGRINS wavelength grid. This stellar model is further smoothed via a Gaussian filter and finally convolved with a broadening kernel to imitate the line broadening from the IGRINS instrument profile. (The Full-Width at Half Maximum of this broadening kernel is given by the ratio of the resolving power of the model spectrum and that of the instrument, which we assume is constant throughout the H and K bands.) The planet-star contrast is then scaled by the planet-star area ratio. Each planet model spectrum is also convolved with an equatorial rotation kernel assuming tidally locked, solid body rotation. (We do not apply additional rotational broadening, such as those originating from 3D effects, as the effects on the line shape would have minimal impact at the resolving power of IGRINS, e.g. the measured excess rotation speed of 1.35



km/s found in ref <sup>31</sup>).

To account for any stretching or shifting of the underlying planet signal during the detrending procedure<sup>28,53</sup>, we apply a final processing step to each planet model spectrum. Before each data-model comparison (either via cross-correlation or likelihood evaluation during the retrieval process), we Doppler shift the model at each phase based on the adopted values for  $K_P$  and  $dV_{\text{sys}}$  and inject it into a noise reduced reconstruction of the data using only the first 6 singular vectors of a given  $N_{\text{frame}} \times N_{\text{pixel}}$  data matrix. We then perform a SVD again on this model-injected matrix to reproduce any alterations to the true planet signal. This last step is crucial to ensure that we apply the same detrending procedure on both the data and the model spectrum. The structure of the atmospheric model is prescribed by an 18 dimensional state vector – 8 elemental abundances along with 10 dimensions from the P-T parameterization. Within our retrieval scheme we also include the planet radial velocity semi-amplitude,  $K_P$ , and deviation from the expected system velocity,  $dV_{\text{sys}}$ , for each observational sequence as nuisance parameters, resulting in a total 22 free parameters.

To sample the posterior distribution, we use a affine invariant ensemble sampler through the python `emcee`<sup>30</sup> package, initializing our sampler with 88 walkers. Our likelihood function is described by the CCF-to-likelihood mapping framework from<sup>28</sup>, which has been utilize in several previous HRCCS studies<sup>14,22,51</sup>, and validated against other likelihood framework developed such as<sup>62</sup> and traditional chi-squared based likelihood approach used on data from the James Webb Space Telescope<sup>25</sup>. The prior ranges assumed for all parameters are detailed in Table 1. We ran the sampler for 10,000 iterations monitoring the autocorrelation length scale, parameter medians, and variance. Running for up to 50,000 iterations changed the nominal metrics by very little. For our analysis, we select the last 1,000 chains, and are left with a set of 88,000 total samples. The full corner plot of the resultant posterior probability distribution is shown in Supplementary Figure 3, alongside the median P-T profile from 1,000 random draws from our sample.

## Gas Detection via Cross-Correlation:

We calculate 2D cross-correlation function (CCF) maps (presented in Fig. 3) as is standard in the high resolution exoplanet spectroscopy literature<sup>24,52</sup>. This is done by calculating the Pearson correlation coefficient between the post-SVD data and an atmospheric model template spectrum Doppler shifted at each orbital phase/spectrum/frame in accordance with the planet’s radial velocity semi-amplitude,  $K_P$ , and a systematic velocity offset,  $dV_{\text{sys}}$ . We do this along a grid of possible  $K_P$  and  $dV_{\text{sys}}$  values, spanning  $200 \text{ km s}^{-1}$  along each velocity dimension centered on the literature value, resulting in 2D maps of correlation coefficients. We quantify the planet signal-to-noise ratio (S/N) by subtracting the median and normalizing by the standard deviation of a  $3\sigma$ -clipped copy of the CCF map, using the *Astropy* function `sigma_clipped_stats`. The calculation of the CCF signal-to-noise using this method has been applied in previous studies,<sup>14</sup> and is warranted

given the large range in  $K_P$  and  $V_{\text{sys}}$  values we explore within the parameter space. The adopted planet detection S/N, i.e., the planet signal detection significance, in this text is the maximum of this normalized CCF map localized around a 25 km/s box centered around the literature planet  $K_P$  and  $V_{\text{sys}}$ . The resultant S/N in most of these strong detections is likely an underestimate of the true detection significance, as, given the level of significance of the detections, the noise structure at  $K_P$ - $V_{\text{sys}}$  pairs far from the peak is likely a mix of both noise and aliased signal.

To search for individual gases, we use the same P-T and gas VMR profiles used to calculate the Fiducial model, but set the abundances of all gases to zero except the specific gas of interest and continuum opacity sources. We then repeat the process and recalculate a high resolution model spectrum and CCF S/N map. The individual detections of Fe I, CO, OH, Mg I, Si I, H<sub>2</sub>O are shown in 3. This marks the second simultaneous detection of both Fe I and Si I in the atmosphere of UHJ in the infrared <sup>63</sup>. The presence of OH is indicative of the thermal dissociation of H<sub>2</sub>O, which may suggest why do not detect water as strongly as other molecules less susceptible to thermal dissociation at these temperatures such as CO. Additionally, the detections of Fe I and Mg I in emission are consistent with previous observations of WASP-189b in transmission <sup>58</sup>.

For CCF maps containing both multiple and single species templates, we consistently find a peak for the cross-correlation function at a  $dV_{\text{sys}}$  of approximately 4 km/s and a  $K_P$  at approximately 193 km/s. This is consistent with our retrieval values where we obtain a  $\delta K_P$  (delta  $K_P$  value) of  $-11.84^{+0.92}_{-0.83}$  and  $-11.71^{+1.77}_{-1.75}$ , and  $dV_{\text{sys}}$  values of  $5.25^{+0.49}_{-0.45}$  and  $2.95^{+0.70}_{-0.57}$  for each night respectively, (see Supplementary Figure 3). Here,  $K_P$  was assumed to have the literature value of  $201 \pm 4$  km/s, calculated using the semi-major axis measurement from <sup>18</sup> and the orbital period from <sup>64</sup>. However, values are in agreement with previous high-resolution thermal emission studies of WASP-189b <sup>31,65</sup>, who measure Keplerian velocities of  $193^{+0.54}_{-2.5}$  km/s and  $193^{+2.4}_{-2.5}$  km/s. <sup>31</sup> also measure a  $\delta V_{\text{sys}}$  offset  $4.7 \pm 0.8$  km/s. While all three measurements of  $K_P$  are offset from the aforementioned literature value, they are well within the uncertainties of the  $K_P$  value quoted in <sup>65</sup>, who calculate  $K_P$  using both the period and semi-major axis from <sup>64</sup>, calculated at  $197^{+15}_{-16}$  km/s.

Searches for individual signal of Ti I, Ca I, V I resulted weak-to-non detections. While there are some lines for these species in the H and K bands, these species have fewer lines in the NIR-Infrared compared to the species which we detect confidently. When we searched for these species using the likelihood formalism of <sup>28</sup> (the same as used in our main retrieval algorithm), as opposed to the traditional Pearson correlation coefficient, these species are seen with tentative significances. This is expected, as the likelihood function is more sensitive to the amplitudes and line-shapes than the traditional correlation coefficient, an effect which has been shown in previous HRCCS gas detections <sup>14</sup>. We show the CCF and log-likelihood detection maps for Ti I, Ca I, V I in the top and bottom rows of Supplementary Figure 2.

## Comparison to Previous Work:

This work joins a growing body of literature studying WASP-189b at high spectral resolution. Most refractory species presented here have been detected previously on WASP-189b by different studies in both the optical <sup>38,66</sup> and in the Near-infrared <sup>31,67</sup>. This work marks the detection of neutral silicon in the atmosphere of this planet, and only the third exoplanet to have neutral silicon detected via thermal emission <sup>27</sup>. One of the most complete chemical inventories of WASP-189b was measured by <sup>38</sup> based on optical transmission data from HARPS and HARPS-N <sup>66</sup>. In contrast to our work, Ref. <sup>38</sup> use a free chemistry modeling prescription in which the volume mixing ratio of each individual gas species is assumed to be constant with pressure. Due to the observed geometry of their analysis (transmission spectrum compared to direct thermal emission), the contribution of their signal originates from the upper atmosphere of the planet, typically probing pressures of 0.1 mbar above an opacity deck <sup>38</sup>. As such, comparison to their work is nontrivial. However, by placing the retrieved enrichment of Fe and Mg from our analysis back into *fastchem*, the code outputs the inferred volume mixing ratios of each gas as a function of pressure. While our analysis is most sensitive to pressures around 0.1 bar, and the transmission spectra of <sup>38</sup> had an opacity deck of 0.1 mbar, the Fe and Mg volume mixing ratios from our main analysis are consistent within the uncertainties to the constant with altitude volume mixing ratios measured by <sup>38</sup>.

Ref. <sup>31</sup> observed WASP-189b during eclipse phases using the CRIRES+ instrument. In their analysis, they perform a chemical equilibrium retrieval similar to ours, (albeit without retrieving for the individual gas enrichment), and find the atmosphere of WASP-189b to be metal enriched, at  $[M/H]_{\odot} = 1.40^{+1.39}_{-0.60}$ , while finding a C/O ratio of  $0.32^{+0.41}_{-0.14}$ . This measurement in metallicity is disparate from our own measurement at  $3\sigma$  confidence, and we attribute this distinction to differences in each analysis, including the wavelength coverage of the data and how the chemical composition of the atmosphere is parameterized. In particular, Ref. <sup>31</sup> parametrizes the atmosphere with  $[M/H]$  (total metallicity defined above) parameter and the Carbon-to-Oxygen ratio. Ref. <sup>31</sup> discusses that the retrieved Oxygen enrichment is linked to the Iron enrichment ( $[O/H] = [Fe/H]$ ) in this parameterization, meaning that there exists a degeneracy between these parameters as a higher metallicity (favored by their model) is correlated with a lower C/O since these values result in low CO abundance. The non-detections of other Oxygen bearing species such as OH or H<sub>2</sub>O in their K-band observations would suggest that their metallicity constraint is primarily driven by the Iron abundance. In contrast, our abundance parameterization, which includes single elemental enrichment factors (e.g., (Fe, Mg, Si...C, O)/H vs. just M/H and C/O), favors an enrichment of Iron relative to Carbon and Oxygen, which in context of <sup>31</sup> could lead to a high metallicity and low C/O. Given these differences, it is non-trivial to draw further conclusions from the discrepancies in the two results.

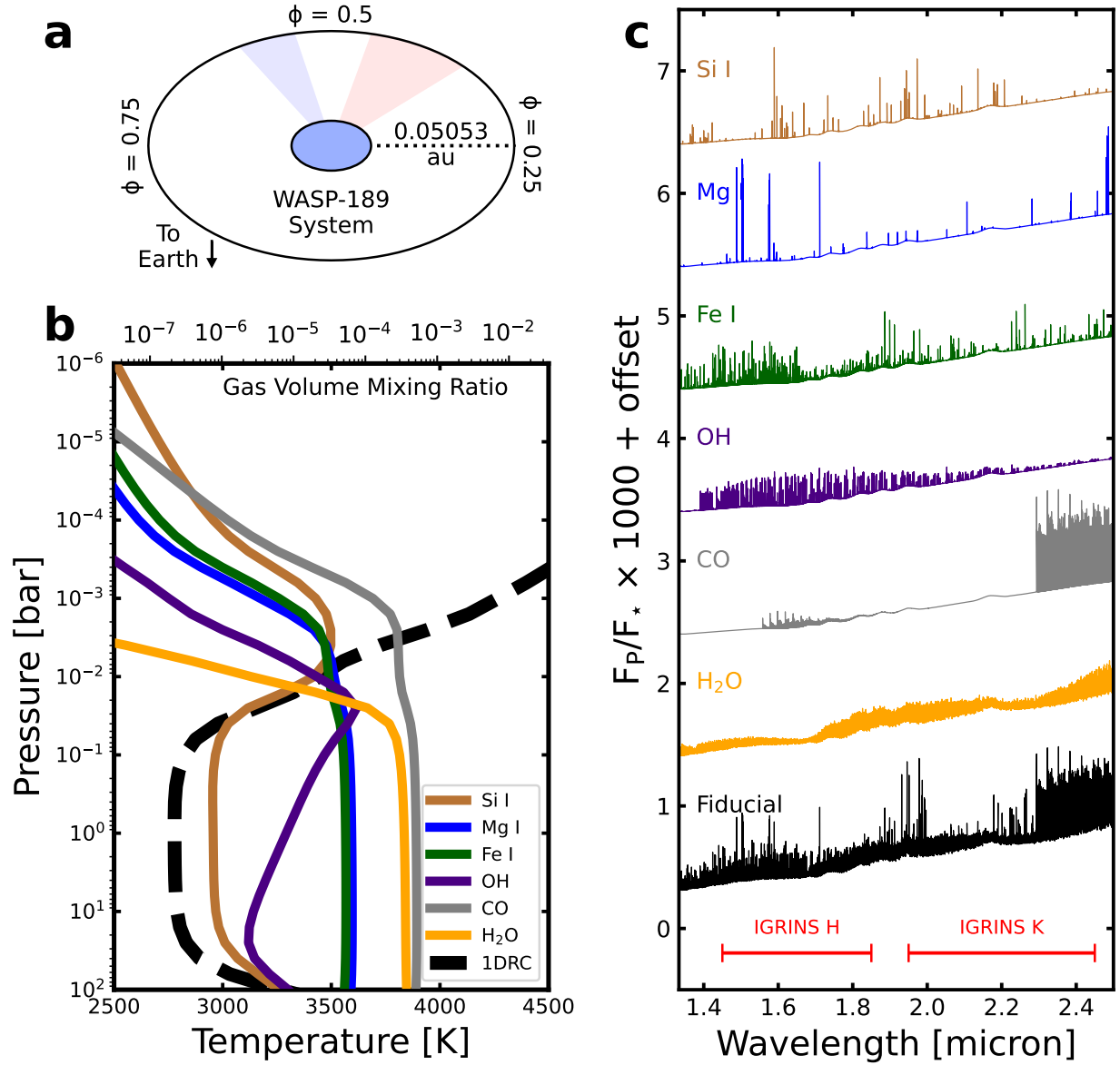


Figure 1: **Observing geometry and model predictions for WASP-189b's atmosphere.** **a** Orbital phase coverage of the IGRINS observations. The pink region shows phases observed in the pre-eclipse dataset and the blue region shows the phases observed after secondary eclipse. **b** Volume-mixing-ratio profiles for selected gases (colored lines, labeled in legend) and predicted thermal structure (black line, labeled 1DRC) based on radiative-convective thermochemical-equilibrium. **c** Model planet-to-star flux ratios illustrating the sensitivity of the IGRINS wavelength range to individual volatile and refractory species. The fiducial spectrum includes all species used in the cross-correlation analysis, and individual model spectra highlight key contributors across the band-pass.

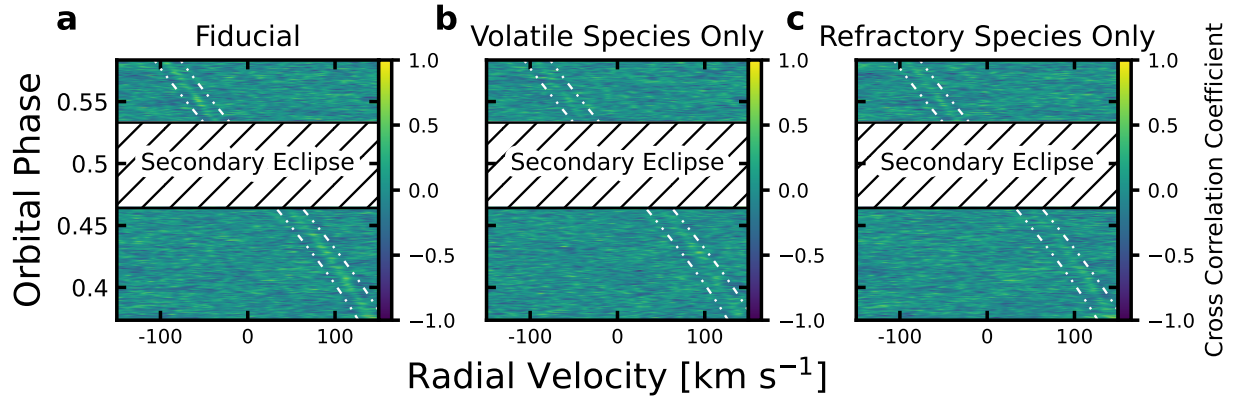


Figure 2: **Cross-correlation coefficient as a function of velocity and orbital phase arising from varying atmospheric model templates.** **a** Fiducial model, including both refractory (Fe I+, Mg I, Si I, Ti I, Ca I, V I) and volatile (H<sub>2</sub>O, CO and OH) species. **b** Model including only refractory species. **c** Model including only volatile species. The colored trails indicate peaks of the cross-correlation function across the orbital phases covered by our observations, indicating a detection of atmospheric emission given that template. The white dashed lines denote  $\pm 15$  km/s offsets from the best fit velocity parameters measured in our atmospheric retrieval analysis. The white box in the middle of each panel indicate the phases during which the planet is blocked by the host star during secondary eclipse.

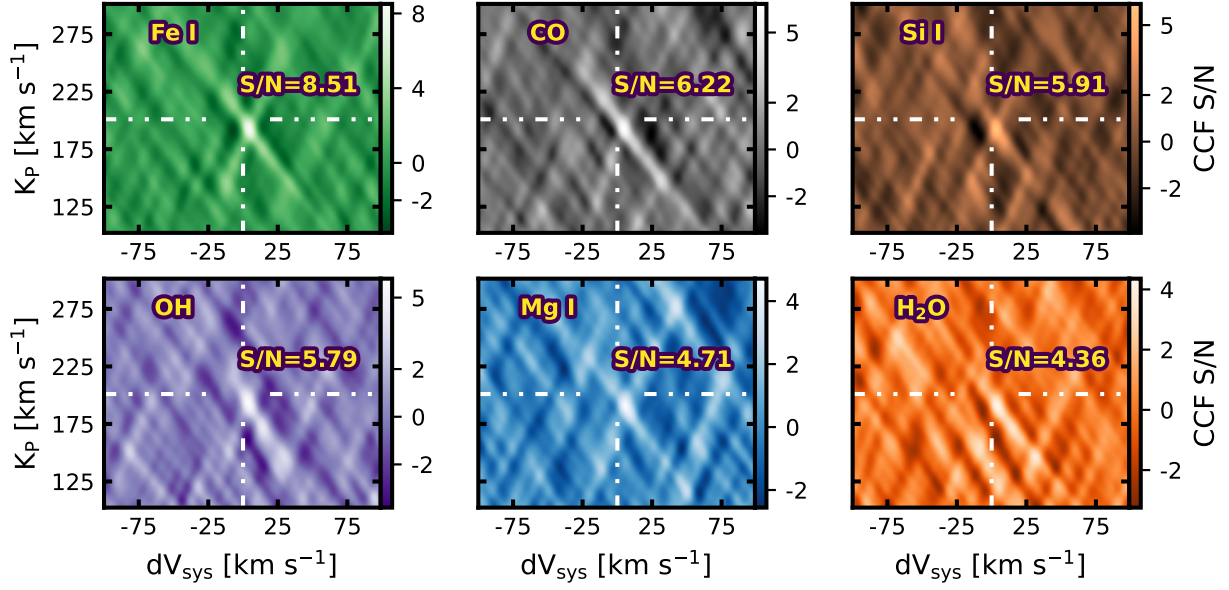


Figure 3: **Cross-correlation signal-to-noise (S/N) ratio maps illustrating the detection of individual species in atmosphere of WASP-189b.** The detected gas for each map is indicated in the upper left of the panel. If that gas is present, a peak occurs near the expected values for the planet’s radial velocity semi-amplitude ( $K_P$ ) and the offset from the star-planet system velocity ( $dV_{\text{sys}}$ )—indicated by the white dot-dashed lines. The S/N for each detection is indicated in each panel.

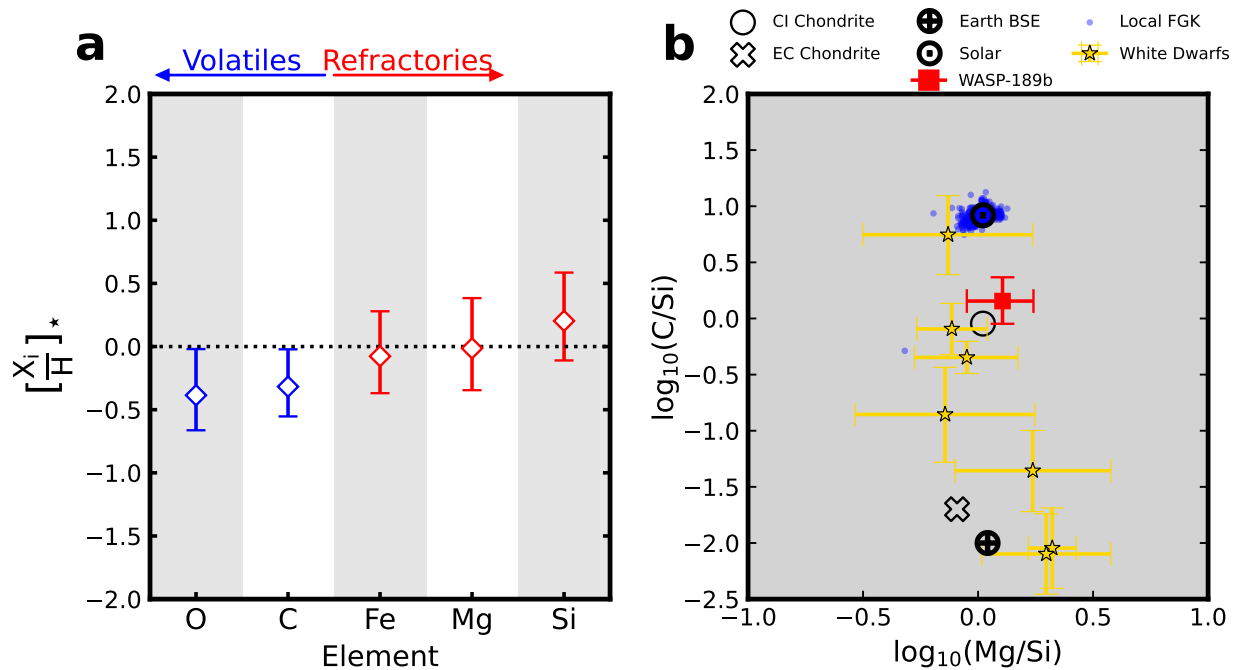


Figure 4: **Elemental abundance estimates and abundance ratios measured in WASP-189b.**  
**a** Abundance estimates for O, C, Fe, Mg, and Si in WASP-189 b relative to those measured in the star,  $[X_i/H]^*$ ,<sup>18</sup>. The errorbar represents the 68 % confidence interval for each measurement. The abundances of O and C are slightly substellar (by just over  $1\sigma$ ), while the refractory species are stellar within  $1\sigma$  uncertainties. **b** Logarithm of the ratio of carbon to silicon measured in different astrophysical objects as a function of the logarithm of the measured magnesium to silicon ratio. The values shown are for the Sun, Bulk Silicate Earth (BSE), CI and EC Chondrites, polluted White Dwarfs (yellow stars), local FGK stars (blue dots) and our measurement of WASP-189b (red square). Errorbars represent the 68 % confidence interval on measurement when shown. The carbon to silicon values for non-stellar objects are from ref<sup>68</sup>. The FGK star values are taken from ref<sup>40</sup>. Figure adapted from ref<sup>41</sup>. The solar value for Mg/Si is assumed as 1.05, while the value for Earth BSE is assumed as 1.10<sup>40,69</sup>. Source data are provided as a Source Data file.

Parameter	Description	Prior Range
[O/H]	Oxygen enrichment relative to solar	$\mathcal{U}(-5,5)$
[C/H]	Carbon enrichment relative to solar	$\mathcal{U}(-5,5)$
[Ca/H]	Calcium enrichment relative to solar	$\mathcal{U}(-5,5)$
[Fe/H]	Iron enrichment to relative solar	$\mathcal{U}(-5,5)$
[Si/H]	Silicon enrichment relative to solar	$\mathcal{U}(-5,5)$
[Ti/H]	Titanium enrichment relative to solar	$\mathcal{U}(-5,5)$
[Mg/H]	Magnesium enrichment relative to solar	$\mathcal{U}(-5,5)$
[V/H]	Vanadium enrichment relative to solar	$\mathcal{U}(-5,5)$
T0	Temperature, Node 1 [K]	$\mathcal{U}(100,6000)$
T1	Temperature, Node 2 [K]	$\mathcal{U}(100,6000)$
T2	Temperature, Node 3 [K]	$\mathcal{U}(100,6000)$
T3	Temperature, Node 4 [K]	$\mathcal{U}(100,6000)$
T4	Temperature, Node 5 [K]	$\mathcal{U}(100,6000)$
T5	Temperature, Node 6 [K]	$\mathcal{U}(100,6000)$
$\log_{10}P_2$	Pressure at Node 2 [bar]	$\mathcal{U}(-6,2.5)$
$\log_{10}P_3$	Pressure at Node 3 [bar]	$\mathcal{U}(-6,2.5)$
$\log_{10}P_4$	Pressure at Node 4 [bar]	$\mathcal{U}(-6,2.5)$
$\log_{10}P_5$	Pressure at Node 5 [bar]	$\mathcal{U}(-6,2.5)$
$dKp_{1,2}$	Difference in Planetary Velocity [km/s]	$\mathcal{U}(-20,20)$
$dV_{sys,1,2}$	Difference in Systemic Velocity [km/s]	$\mathcal{U}(-20,20)$

Table 1: **Description of the retrieved parameters and their prior ranges.** The first column gives the title of each parameter in our main retrieval algorithm. Column 2 is the description of each parameter along with the associated units. Column 3 gives the prior ranges for each of these parameters.



**Data Availability** This work is based on observations made with the Gemini South Telescope. The raw data products are available within the Gemini Observatory Archive. The data generated and analyzed in this study, including reduced data cubes, model spectra, files used to generate cross correlation maps and the main retrieval outputs have been deposited in following Zenodo repository via doi:10.5281/zenodo.17875072. References to the solar/stellar abundances used in this analysis are cited within the manuscript. Source data are provided with this paper.

**Code Availability** The cross-correlation analysis and retrieval codes used in this analysis are based upon that presented in Ref. <sup>21</sup>, with the relevant links to these codes in that manuscript. The data products used in the analysis were reduced using the `cubify` package: <https://zenodo.org/records/14194202>. The code also made use of the publicly available `fastchem` tool <sup>56</sup>: <https://github.com/NewStrangeWorlds/FastChem>.

1. Guillot, T. *et al.* Giant Planets from the Inside-Out. In Inutsuka, S., Aikawa, Y., Muto, T., Tomida, K. & Tamura, M. (eds.) *Protostars and Planets VII*, vol. 534 of *Astronomical Society of the Pacific Conference Series*, 947 (2023).
2. Venturini, J. & Helled, R. Jupiter’s heavy-element enrichment expected from formation models. *A&A* **634**, A31 (2020). 1911.12767.
3. Madhusudhan, N. Exoplanetary Atmospheres: Key Insights, Challenges, and Prospects. *ARA&A* **57**, 617–663 (2019). 1904.03190.
4. Öberg, K. I., Murray-Clay, R. & Bergin, E. A. The Effects of Snowlines on C/O in Planetary Atmospheres. *ApJL* **743**, L16 (2011). 1110.5567.
5. Madhusudhan, N. C/O Ratio as a Dimension for Characterizing Exoplanetary Atmospheres. *ApJ* **758**, 36 (2012). 1209.2412.
6. Cridland, A. J., Pudritz, R. E. & Alessi, M. Composition of early planetary atmospheres - I. Connecting disc astrochemistry to the formation of planetary atmospheres. *MNRAS* **461**, 3274–3295 (2016). 1605.09407.
7. Mordasini, C., van Boekel, R., Mollière, P., Henning, T. & Benneke, B. The Imprint of Exoplanet Formation History on Observable Present-day Spectra of Hot Jupiters. *ApJ* **832**, 41 (2016). 1609.03019.
8. Kempton, E. M. R. & Knutson, H. A. Transiting Exoplanet Atmospheres in the Era of JWST. *Reviews in Mineralogy and Geochemistry* **90**, 411–464 (2024). 2404.15430.
9. Lichtenberg, T. & Krijt, S. System-level Fractionation of Carbon from Disk and Planetesimal Processing. *ApJL* **913**, L20 (2021). 2105.06159.
10. Lothringer, J. D. *et al.* A New Window into Planet Formation and Migration: Refractory-to-Volatile Elemental Ratios in Ultra-hot Jupiters. *ApJ* **914**, 12 (2021). 2011.10626.

11. Chachan, Y., Knutson, H. A., Lothringer, J. & Blake, G. A. Breaking Degeneracies in Formation Histories by Measuring Refractory Content in Gas Giants. *ApJ* **943**, 112 (2023). 2211.09080.
12. Thiabaud, A., Marboeuf, U., Alibert, Y., Leya, I. & Mezger, K. Elemental ratios in stars vs planets. *A&A* **580**, A30 (2015). 1507.01343.
13. Pelletier, S. *et al.* CRIRES<sup>+</sup> and ESPRESSO Reveal an Atmosphere Enriched in Volatiles Relative to Refractories on the Ultrahot Jupiter WASP-121b. *AJ* **169**, 10 (2025). 2410.18183.
14. Smith, P. C. B. *et al.* The Roasting Marshmallows Program with IGRINS on Gemini South. II. WASP-121 b has Superstellar C/O and Refractory-to-volatile Ratios. *AJ* **168**, 293 (2024). 2410.19017.
15. Dorn, C., Hinkel, N. R. & Venturini, J. Bayesian analysis of interiors of HD 219134b, Kepler-10b, Kepler-93b, CoRoT-7b, 55 Cnc e, and HD 97658b using stellar abundance proxies. *A&A* **597**, A38 (2017). 1609.03909.
16. Unterborn, C. T. & Panero, W. R. The Effects of Mg/Si on the Exoplanetary Refractory Oxygen Budget. *ApJ* **845**, 61 (2017). 1604.08309.
17. Spaargaren, R. J., Ballmer, M. D., Bower, D. J., Dorn, C. & Tackley, P. J. The influence of bulk composition on the long-term interior-atmosphere evolution of terrestrial exoplanets. *A&A* **643**, A44 (2020). 2007.09021.
18. Lendl, M. *et al.* The hot dayside and asymmetric transit of WASP-189 b seen by CHEOPS. *A&A* **643**, A94 (2020). 2009.13403.
19. Deline, A. *et al.* The atmosphere and architecture of WASP-189 b probed by its CHEOPS phase curve. *A&A* **659**, A74 (2022). 2201.04518.
20. Park, C. *et al.* Design and early performance of IGRINS (Immersion Grating Infrared Spectrometer). In Ramsay, S. K., McLean, I. S. & Takami, H. (eds.) *Ground-based and Airborne Instrumentation for Astronomy V*, vol. 9147 of *Society of Photo-Optical Instrumentation Engineers (SPIE) Conference Series*, 91471D (2014).
21. Line, M. R. *et al.* A solar c/o and sub-solar metallicity in a hot jupiter atmosphere. *Nature* **598**, 580–584 (2021).
22. Brogi, M. *et al.* The Roasting Marshmallows Program with IGRINS on Gemini South I: Composition and Climate of the Ultrahot Jupiter WASP-18 b. *AJ* **165**, 91 (2023). 2209.15548.
23. Snellen, I. A. G., de Kok, R. J., de Mooij, E. J. W. & Albrecht, S. The orbital motion, absolute mass and high-altitude winds of exoplanet HD209458b. *Nature* **465**, 1049–1051 (2010). 1006.4364.

24. Birkby, J. L. Exoplanet Atmospheres at High Spectral Resolution. *arXiv e-prints* arXiv:1806.04617 (2018). 1806.04617.
25. Smith, P. C. B. *et al.* A Combined Ground-based and JWST Atmospheric Retrieval Analysis: Both IGRINS and NIRSpec Agree that the Atmosphere of WASP-77A b Is Metal-poor. *AJ* **167**, 110 (2024). 2312.13069.
26. Ramkumar, S., Gibson, N. P., Nugroho, S. K., Maguire, C. & Fortune, M. High-resolution emission spectroscopy retrievals of MASCARA-1b with CRIRES+: strong detections of CO, H<sub>2</sub>O, and Fe emission lines and a C/O consistent with solar. *MNRAS* **525**, 2985–3005 (2023). 2308.07157.
27. Cont, D. *et al.* Silicon in the dayside atmospheres of two ultra-hot Jupiters. *A&A* **657**, L2 (2022). 2112.10461.
28. Brogi, M. & Line, M. R. Retrieving temperatures and abundances of exoplanet atmospheres with high-resolution cross-correlation spectroscopy. *AJ* **157**, 114 (2019).
29. Gibson, N. P. *et al.* Detection of Fe I in the atmosphere of the ultra-hot Jupiter WASP-121b, and a new likelihood-based approach for Doppler-resolved spectroscopy. *MNRAS* **493**, 2215–2228 (2020). 2001.06430.
30. Foreman-Mackey, D., Hogg, D. W., Lang, D. & Goodman, J. emcee: the mcmc hammer. *Publications of the Astronomical Society of the Pacific* **125**, 306 (2013).
31. Lesjak, F. *et al.* Retrieving wind properties from the ultra-hot dayside of WASP-189b with CRIRES<sup>+</sup>. *arXiv e-prints* arXiv:2411.19662 (2024). 2411.19662.
32. Stock, J. W., Kitzmann, D., Patzer, A. B. C. & Sedlmayr, E. FastChem: A computer program for efficient complex chemical equilibrium calculations in the neutral/ionized gas phase with applications to stellar and planetary atmospheres. *MNRAS* **479**, 865–874 (2018). 1804.05010.
33. Kopparapu, R. k., Kasting, J. F. & Zahnle, K. J. A Photochemical Model for the Carbon-rich Planet WASP-12b. *ApJ* **745**, 77 (2012). 1110.2793.
34. Moses, J. I., Madhusudhan, N., Visscher, C. & Freedman, R. S. Chemical Consequences of the C/O Ratio on Hot Jupiters: Examples from WASP-12b, CoRoT-2b, XO-1b, and HD 189733b. *ApJ* **763**, 25 (2013). 1211.2996.
35. Lothringer, J. D., Barman, T. & Koskinen, T. Extremely Irradiated Hot Jupiters: Non-Oxide Inversions, H- Opacity, and Thermal Dissociation of Molecules. *ArXiv e-prints: 1805.00038* (2018). 1805.00038.
36. Asplund, M., Amarsi, A. M. & Grevesse, N. The chemical make-up of the Sun: A 2020 vision. *A&A* **653**, A141 (2021). 2105.01661.

37. Pelletier, S. *et al.* Vanadium oxide and a sharp onset of cold-trapping on a giant exoplanet. *Nature* **619**, 491–494 (2023). 2306.08739.
38. Gandhi, S. *et al.* Retrieval Survey of Metals in Six Ultrahot Jupiters: Trends in Chemistry, Rain-out, Ionization, and Atmospheric Dynamics. *AJ* **165**, 242 (2023). 2305.17228.
39. Dorn, C. *et al.* Can we constrain the interior structure of rocky exoplanets from mass and radius measurements? *A&A* **577**, A83 (2015). 1502.03605.
40. Brewer, J. M. & Fischer, D. A. C/O and Mg/Si Ratios of Stars in the Solar Neighborhood. *ApJ* **831**, 20 (2016).
41. Zuckerman, B. & Young, E. Characterizing the chemistry of planetary materials around white dwarf stars. In *Handbook of Exoplanets*, 1–22 (Springer, 2017).
42. Xu, S. *et al.* Compositions of Planetary Debris around Dusty White Dwarfs. *AJ* **158**, 242 (2019). 1910.07197.
43. Johnson, T. M. *et al.* Unusual Abundances from Planetary System Material Polluting the White Dwarf G238-44. *ApJ* **941**, 113 (2022). 2211.02673.
44. Rogers, L. K. *et al.* Seven white dwarfs with circumstellar gas discs II: tracing the composition of exoplanetary building blocks. *MNRAS* **532**, 3866–3880 (2024). 2406.11470.
45. Bonsor, A. *et al.* Host-star and exoplanet compositions: a pilot study using a wide binary with a polluted white dwarf. *MNRAS* **503**, 1877–1883 (2021). 2102.02843.
46. Lodders, K. Solar System Abundances and Condensation Temperatures of the Elements. *ApJ* **591**, 1220–1247 (2003).
47. Adibekyan, V. *et al.* A compositional link between rocky exoplanets and their host stars. *Science* **374**, 330–332 (2021). 2102.12444.
48. Spaargaren, R. J., Ballmer, M. D., Bower, D. J., Dorn, C. & Tackley, P. J. The influence of bulk composition on the long-term interior-atmosphere evolution of terrestrial exoplanets. *A&A* **643**, A44 (2020). 2007.09021.
49. Mace, G. *et al.* IGRINS at the Discovery Channel Telescope and Gemini South. In Evans, C. J., Simard, L. & Takami, H. (eds.) *Ground-based and Airborne Instrumentation for Astronomy VII*, vol. 10702 of *Society of Photo-Optical Instrumentation Engineers (SPIE) Conference Series*, 107020Q (2018).
50. Lee, J.-J. & Gullikson, K. Plp: V2.1 Alpha 3 (2016).
51. Kanumalla, K. *et al.* IGRINS Observations of WASP-127 b: H<sub>2</sub>O, CO, and Super-solar Atmospheric Metallicity in the Inflated Sub-Saturn. *AJ* **168**, 201 (2024). 2406.14072.

52. de Kok, R. J. *et al.* Detection of carbon monoxide in the high-resolution day-side spectrum of the exoplanet HD 189733b. *A&A* **554**, A82 (2013). 1304.4014.
53. Gibson, N. P., Nugroho, S. K., Lothringer, J., Maguire, C. & Sing, D. K. Relative abundance constraints from high-resolution optical transmission spectroscopy of WASP-121b, and a fast model-filtering technique for accelerating retrievals. *MNRAS* **512**, 4618–4638 (2022). 2201.04025.
54. Fortney, J. J., Lodders, K., Marley, M. S. & Freedman, R. S. A Unified Theory for the Atmospheres of the Hot and Very Hot Jupiters: Two Classes of Irradiated Atmospheres. *ApJ* **678**, 1419–1435 (2008). 0710.2558.
55. Arcangeli, J. *et al.* Climate of an ultra hot Jupiter. Spectroscopic phase curve of WASP-18b with HST/WFC3. *A&A* **625**, A136 (2019). 1904.02069.
56. Stock, J. W., Kitzmann, D. & Patzer, A. B. C. FASTCHEM 2 : an improved computer program to determine the gas-phase chemical equilibrium composition for arbitrary element distributions. *MNRAS* **517**, 4070–4080 (2022). 2206.08247.
57. Borsato, N. W. *et al.* The Mantis Network. III. Expanding the limits of chemical searches within ultra-hot Jupiters: New detections of Ca I, V I, Ti I, Cr I, Ni I, Sr II, Ba II, and Tb II in KELT-9 b. *A&A* **673**, A158 (2023). 2304.04285.
58. Prinoth, B. *et al.* An atlas of resolved spectral features in the transmission spectrum of WASP-189 b with MAROON-X. *A&A* **685**, A60 (2024). 2403.08863.
59. Bell, T. J. *et al.* Nightside clouds and disequilibrium chemistry on the hot Jupiter WASP-43b. *Nature Astronomy* **8**, 879–898 (2024). 2401.13027.
60. Grimm, S. L. *et al.* HELIOS-K 2.0 Opacity Calculator and Open-source Opacity Database for Exoplanetary Atmospheres. *ApJS* **253**, 30 (2021). 2101.02005.
61. Husser, T. O. *et al.* A new extensive library of PHOENIX stellar atmospheres and synthetic spectra. *A&A* **553**, A6 (2013). 1303.5632.
62. Gibson, N. P. *et al.* Detection of Fe I in the atmosphere of the ultra-hot Jupiter WASP-121b, and a new likelihood-based approach for Doppler-resolved spectroscopy. *MNRAS* **493**, 2215–2228 (2020). 2001.06430.
63. Cont, D. *et al.* Atmospheric characterization of the ultra-hot Jupiter WASP-33b. Detection of Ti and V emission lines and retrieval of a broadened line profile. *A&A* **668**, A53 (2022). 2209.10618.
64. Anderson, D. R. *et al.* WASP-189b: an ultra-hot Jupiter transiting the bright A star HR 5599 in a polar orbit. *arXiv e-prints* arXiv:1809.04897 (2018). 1809.04897.

65. Yan, F. *et al.* Detection of iron emission lines and a temperature inversion on the dayside of the ultra-hot Jupiter KELT-20b. *A&A* **659**, A7 (2022). 2201.08759.
66. Prinoth, B. *et al.* Titanium oxide and chemical inhomogeneity in the atmosphere of the exoplanet WASP-189 b. *Nature Astronomy* **6**, 449–457 (2022). 2111.12732.
67. Yan, F. *et al.* Detection of CO emission lines in the dayside atmospheres of WASP-33b and WASP-189b with GIANO. *A&A* **661**, L6 (2022). 2204.10158.
68. Bergin, E. A., Blake, G. A., Ciesla, F., Hirschmann, M. M. & Li, J. Tracing the ingredients for a habitable earth from interstellar space through planet formation. *Proceedings of the National Academy of Science* **112**, 8965–8970 (2015). 1507.04756.
69. Allègre, C. J., Poirier, J.-P., Humler, E. & Hofmann, A. W. The chemical composition of the Earth. *Earth and Planetary Science Letters* **134**, 515–526 (1995).
70. Karman, T. *et al.* Update of the HITRAN collision-induced absorption section. *Icarus* **328**, 160–175 (2019).
71. Polyansky, O. L. *et al.* ExoMol molecular line lists XXX: a complete high-accuracy line list for water. *MNRAS* **480**, 2597–2608 (2018). 1807.04529.
72. Li, G. *et al.* Rovibrational Line Lists for Nine Isotopologues of the CO Molecule in the X  $^1\Sigma^+$  Ground Electronic State. *ApJS* **216**, 15 (2015).
73. Rothman, L. S. *et al.* HITEMP, the high-temperature molecular spectroscopic database. *J. Quant. Spec. Radiat. Transf.* **111**, 2139–2150 (2010).
74. Kurucz, R. L. Including All the Lines: Data Releases for Spectra and Opacities through 2017. In *Workshop on Astrophysical Opacities*, vol. 515 of *Astronomical Society of the Pacific Conference Series*, 47 (2018).
75. John, T. L. Continuous absorption by the negative hydrogen ion reconsidered. *A&A* **193**, 189–192 (1988).
76. Arcangeli, J. *et al.* H $^-$  Opacity and Water Dissociation in the Dayside Atmosphere of the Very Hot Gas Giant WASP-18b. *ApJL* **855**, L30 (2018). 1801.02489.
77. Bell, T. J. & Cowan, N. B. Increased Heat Transport in Ultra-hot Jupiter Atmospheres through H $_2$  Dissociation and Recombination. *ApJL* **857**, L20 (2018). 1802.07725.
78. Mansfield, M. *et al.* A unique hot Jupiter spectral sequence with evidence for compositional diversity. *Nature Astronomy* **5**, 1224–1232 (2021). 2110.11272.
79. Saffe, C. *et al.* Chemical analysis of early-type stars with planets. *A&A* **647**, A49 (2021). 2101.04416.

80. Lam, M. B., Hoeijmakers, H. J., Prinoth, B. & Thorsbro, B. Secrets in the shadow: High precision stellar abundances of fast-rotating A-type exoplanet host stars through transit spectroscopy. *A&A* **691**, A141 (2024). 2409.15951.
81. Asplund, M., Grevesse, N., Sauval, A. J. & Scott, P. The Chemical Composition of the Sun. *ARA&A* **47**, 481–522 (2009). 0909.0948.
82. Yan, F. *et al.* A temperature inversion with atomic iron in the ultra-hot dayside atmosphere of WASP-189b. *A&A* **640**, L5 (2020). 2007.02716.
83. Wakeford, H. R. *et al.* HAT-P-26b: A Neptune-mass exoplanet with a well-constrained heavy element abundance. *Science* **356**, 628–631 (2017). 1705.04354.
84. Visscher, C., Lodders, K. & Fegley, B., Jr. Atmospheric Chemistry in Giant Planets, Brown Dwarfs, and Low-mass Dwarf Stars. III. Iron, Magnesium, and Silicon. *ApJ* **716**, 1060–1075 (2010). 1001.3639.
85. Lee, E. K. H. *et al.* The Mantis Network II: examining the 3D high-resolution observable properties of the UHJs WASP-121b and WASP-189b through GCM modelling. *MNRAS* **517**, 240–256 (2022). 2210.11986.
86. Prinoth, B. *et al.* Time-resolved transmission spectroscopy of the ultra-hot Jupiter WASP-189 b. *A&A* **678**, A182 (2023). 2308.04523.
87. Wang, Y., lin Zhou, J., hui gen, L. & Meng, Z. Forming different planetary architectures. i. the formation efficiency of hot jupiters from high-eccentricity mechanisms. *The Astrophysical Journal* **848**, 20 (2017). URL <https://dx.doi.org/10.3847/1538-4357/aa8868>.
88. Albrecht, S. H., Dawson, R. I. & Winn, J. N. Stellar Obliquities in Exoplanetary Systems. *PASP* **134**, 082001 (2022). 2203.05460.
89. Rice, M., Wang, S. & Laughlin, G. Origins of Hot Jupiters from the Stellar Obliquity Distribution. *ApJL* **926**, L17 (2022). 2201.11768.
90. Fortney, J. J., Dawson, R. I. & Komacek, T. D. Hot Jupiters: Origins, Structure, Atmospheres. *Journal of Geophysical Research (Planets)* **126**, e06629 (2021). 2102.05064.
91. Lothringer, J. D. *et al.* Refractory and Volatile Species in the UV-to-IR Transmission Spectrum of Ultra-hot Jupiter WASP-178b with HST and JWST. *AJ* **169**, 274 (2025). 2503.15472.

**Acknowledgements** J.A.S., M.R.L, S.K.K and J.L.B acknowledge support from NSF grant AST-2307177/8. P.C.B.S acknowledges support provided by NASA through the NASA FINESST grant 80NSSC22K1598. L.W. and M.W.M. acknowledge support through the 51 Pegasi b Fellowship awarded by the Heising-Simons Foundation. The results reported herein benefited from collaborations and/or information exchange

within NASA’s Nexus for Exoplanet System Science (NExSS) research coordination network sponsored by NASA’s Science Mission Directorate, grant 80NSSC23K1356, PI Steve Desch. This material is based upon work supported by the National Science Foundation under grant MSIP-1836008. We acknowledge Research Computing at Arizona State University for providing high-performance computing and storage resources that have significantly contributed to the research results reported within this manuscript. This work used the Immersion Grating Infrared Spectrometer (IGRINS) that was developed under a collaboration between the University of Texas at Austin and the Korea Astronomy and Space Science Institute (KASI) with the financial support of the Mount Cuba Astronomical Foundation, of the US National Science Foundation under grants AST-1229522 and AST-1702267, of the McDonald Observatory of the University of Texas at Austin, of the Korean GMT Project of KASI, and Gemini Observatory. This program is based on observations obtained at the international Gemini Observatory, a program of NSF’s NOIRLab, which is managed by the Association of Universities for Research in Astronomy (AURA) under a cooperative agreement with the National Science Foundation on behalf of the Gemini Observatory partnership: the National Science Foundation (United States), National Research Council (Canada), Agencia Nacional de Investigación y Desarrollo (Chile), Ministerio de Ciencia, Tecnología e Innovación (Argentina), Ministério da Ciência, Tecnologia, Inovações e Comunicações (Brazil), and Korea Astronomy and Space Science Institute (Republic of Korea). J.A.S and M.R.L would especially like to thank the anonymous queue observers who successfully completed the observing programs this work is based on. We would like to thank Monika Lendl for useful discussion on stellar abundance analyses. Finally, we also acknowledge the wonderful journal cover art by Hailey Nelson.

**Author Contributions** J.A.S. performed the analysis, wrote the manuscript, and prepared one of the proposals that resulted in the post-eclipse dataset. P.C.B.S. developed code, contributed text to the manuscript, provided scientific guidance, and reviewed the paper. K.K. performed additional retrieval analyses and integrated the `fastchem` code into the CHIMERA retrieval pipeline. L.W. provided scientific input, guided J.A.S. throughout the writing process, and advised on manuscript focus. M.R.L. conceived the paper, wrote the original Gemini L.L.P. proposal from which the pre-eclipse dataset originates, edited and revised the manuscript, and supervised J.A.S. throughout the project. S.P. provided code and spectral comparisons that helped identify a bug in the atomic opacities. S.D., P.Y., and J.P. provided comments on multiple drafts and scientific guidance on planetary formation and composition. J.B., M.B., D.J., and G.N.M. contributed to the development and operation of IGRINS and its associated data pipeline. M.W.M. and A.B.S. contributed to data analysis, retrieval tests, and manuscript comments. V.P., L.P., L.v.S., and J.P.W. provided theoretical context on atmospheric chemistry and manuscript feedback. All authors read and approved the final version of the manuscript and contributed to the discussion of results.

**Competing interests** The authors declare no competing interests.



## Supplementary Information

### Supplementary Note 1: Sources of Opacity Line Lists

The opacity line-lists used in the main analysis come from the following sources; CIA from <sup>70</sup>; H<sub>2</sub>O from EXOMOL <sup>71</sup>; CO and OH from the HITEMP database <sup>72,73</sup>; neutral atomic species from the Kurucz line database (gfall2017) <sup>74</sup>, H<sup>-</sup> from <sup>75</sup>.

### Supplementary Discussion

The full corner plot of our main atmospheric retrieval is shown in Supplementary Figure 3. Each of the 22 parameters in our model is shown on the left. Supplementary Figure 4 shows the median P-T profile along with 1 and 2  $\sigma$  confidence interval generated from 1000 random draws of the posterior probability distribution. We also compare our retrieved profile with another model generated under 1D radiative-convective-thermochemical equilibrium, similar to ref's <sup>76–78</sup>, and find that they are in strong agreement with another.

All the gases in our chemical parametrization show bounded measurements with their 68% confidence intervals. While this is expected given our strong detections in the CCF maps for most species, we note that the constraints achieved on Ti I, Ca I, V I can be also be attributed to their stronger detections using the likelihood function, as seen in the logL S/N maps on bottom row Supplementary Figure 2. As noted in previous HRCCS studies such as refs <sup>21</sup> and <sup>14</sup>, species with weak-to-non detections using traditional CCF maps have had constrained abundance measurements within a retrieval framework due to the greater sensitivity of the log-likelihood function to line amplitudes and line shapes. Because the gases are output from the retrieval based on equation 1 of the main text (relative to the solar values from ref <sup>36</sup>) we calculate the  $\log_{10}(\frac{X}{H})$  value for each individual gas by adding the  $\log_{10}(\frac{X}{H})$  solar value from <sup>36</sup>. This allows us to calculate relative quantities such as the carbon-to-oxygen and refractory-to-refractory ratios, but to also to compare these derived quantities in the planet with literature stellar values.

As mentioned in the main text, our main source of stellar chemical abundances is cited from ref <sup>18</sup>. For all species with listed stellar measurement uncertainties, we propagate these uncertainties into our calculations by generating arrays of random values from a normal distribution centered at the stellar abundance, with a standard deviation the size of the measurement uncertainty from <sup>18</sup>. We use these arrays as the stellar values from which to compare to our planet measurements. Since the listed C and O abundance in WASP-189 from <sup>18</sup> are presented without uncertainties, we apply an uncertainty of 0.13 dex for each, the same uncertainty level listed for the [Fe/H] value.

We note the difficulty in measuring stellar abundances, and in particular for A type stars such as WASP-189. There exist other measured stellar chemical patterns for the host star besides those presented in <sup>18</sup>, such as from <sup>79</sup> and <sup>80</sup>, the latter whose work was done in an effort to try and mitigate the rotational effects on the stellar spectrum of WASP-189. However, not all of retrieved gases in our model have measured stellar values in these studies. We therefore elect to quote the values listed <sup>18</sup> for its measurement of both refractory elements as well as Carbon and Oxygen. Should the stellar parameters be updated in the future, the updated calculations of planet-to-stellar ratios is straightforward.

The first column of 1 shows each gas considered in our model, followed by the log abundance of this element relative to Hydrogen in the atmosphere of WASP-189b as measured in our retrieval analysis. Subsequent columns include the  $\log_{10}(X/H)$  ratio for each element  $X$  with respect to solar or stellar literature values for the abundances of these species. Column 3 contains the retrieved enrichment relative to the solar value <sup>36</sup>  $[X/H]_{\odot}$  (main output of the retrieval). Column 4,  $[X/H]_{*L20}$ , are these values relative to the abundances presented in <sup>18</sup>, which is the stellar abundance pattern we consider in our main results. Column 5 shows the elemental enrichment relative to <sup>79</sup>,  $[X/H]_{*S21}$ , and finally column 6 from ref <sup>80</sup>,  $[X/H]_{*La21}$ . When the stellar abundance is listed with an uncertainty, we propagate the error bar into our  $[X/H]$  value as done with the values from <sup>18</sup> in our main result. If the species is not reported in the respective reference, it is not listed in the table.

As a robustness check for our measured Mg/Si ratio on WASP-189b, we derive the  $\log_{10}\left(\frac{(Mg/Si)}{(Mg/Si)_*}\right)$  against some of the different Mg/Si measurements referenced in the main text. These include the solar value <sup>81</sup>, the stellar values reported from both <sup>18,79</sup> and the local FGK population. This is shown in Supplementary Figure 5. Our calculated Mg/Si ratio is consistent against different sets of measured stellar abundances containing both Mg and Si, as well as the solar and local stellar deviations.

The pressure-temperature profile scheme adopted in our analysis has been utilized previously in <sup>14</sup>, albeit with a slight different configuration. As predicted from the day-side of ultra-hot Jupiters <sup>54</sup>, our retrieval favors a thermal inversion, where the temperature begins to increase with pressure past a certain point. This is consistent with secondary eclipse measurements of ultra-hot Jupiters <sup>14,22,26</sup> including analysis previous performed on WASP-189b <sup>31,82</sup>.

Our thermal structure favors a highly irradiated day-side where we would not expect cloud or condensate formation to effect our abundance constraints. To illustrate this point, in Supplementary Figure 6 we plot our pressure-temperature profile from Supplementary Figure 4 alongside condensation curves for major condensates containing Fe, Si, Mg, Ti and Ca calculated using our retrieved metallicity and the P-T relations from ref's <sup>83,84</sup>. Our profile does not cross any of these major condensate lines, suggesting that our abundances constraints are not biased by Fe, Mg or Si condensing in the day of the planet. As a further check, we also plot day-side and night-side

PT profiles as output from the Global Circulation Models (GCM) for WASP-189b computed in <sup>85</sup>. These models account for 3 dimensional effects on exoplanet atmospheres to understand the chemistry and climate processes on these planets. Encouragingly, our retrieved thermal profile is in agreement with the day-side TP profile from the post-proceeded WASP-189b GCM. Moreover, the night-side TP profile is predicted to be hot enough to also not cross these condensation curves of Fe,Mg or Si bearing species meaning that even the night-side of the planet should not be effected by any major cold-trapping of Fe, Si or Mg. This is further supported by the detection and measurement of these neutral Fe and Mg in transmission <sup>38,66,86</sup>.

We determine the volatile-to-refractory ratio (R/V) by adding the contributions from volatile (O and C) and refractory (Fe, Si ,Mg ,Ti , Ca , V) elements. Upon doing so, we obtain a slightly super-stellar refractory to volatile ratio of  $[R/V]_* = 0.38^{+0.18}_{-0.19}$ , with individual refractory to oxygen and refractory to carbon ratios also slightly super-stellar. Fig. 7 shows how our measured refractory and volatile content coincide with the disk modeling framework developed by <sup>11</sup> to predict the formation location of giant planets. This shows the total sum of the refractory species relative to Hydrogen (relative to stellar) against oxygen (panel a, left) and carbon (panel b, right) to total refractory content (again relative to stellar). The different colored lines correspond to predictions from <sup>11</sup> of these values based on formation location as designated by the legend on the top. Our 2D histograms of these quantities derived from our retrieval results are plotted alongside these colored lines.

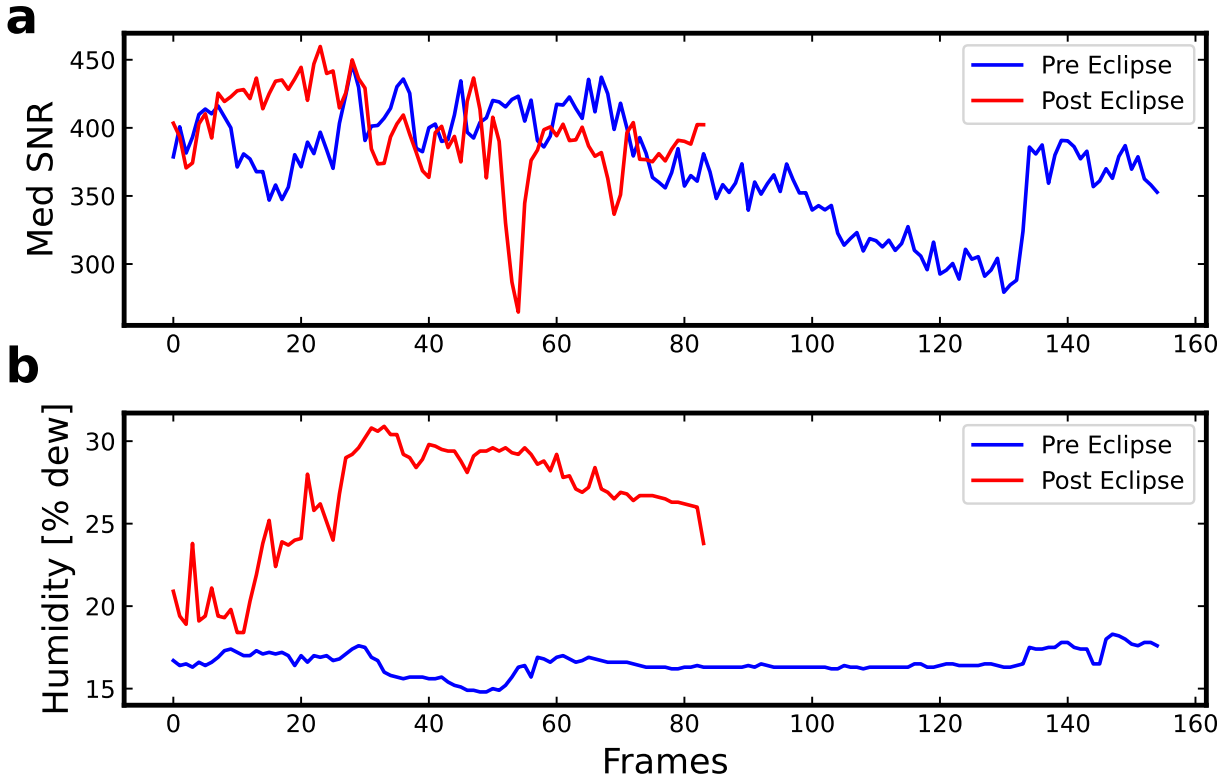
Given the measured  $[R/H]_*$  of  $0.01^{+0.36}_{-0.29}$ , which is a proxy for the solid-to-gas accretion, along with our metallicity and C/O ratios being consistent with the stellar values 68% confidence, our results are consistent within a number of formation pathways within the disk modeling framework presented in ref <sup>11</sup>. The stellar  $[R/H]_*$  value is indicative of a balanced mix of solid and gas accretion, while the moderately O/R and C/R ratios suggest that these solids were slightly elevated in rocky solids as compared to ices. These values are consistent with formation interior to the snow lines, where the planetesimal pollution would be more rich in refractory species than volatiles.

Formation interior to the CO snow line is also supported by our stellar/solar value for the ratio of Carbon-to-Oxygen. However, given that our measured R/V ratio is consistent with the stellar value at  $2\sigma$ , we cannot rule out formation beyond the CO snow line. The latter case would require WASP-189b to migrate 10's of AU after formation to its final orbital location of  $0.05053 \pm 0.00098$  AU. Such a large migration pathway toward the interior of the disk may have given rise to the near-polar orbit (the obliquity  $86.4^{+2.9}_{-4.4}$  degrees, <sup>18</sup>) seen in the WASP-189b system, although there are several mechanisms that are thought to cause the misaligned spin-orbit angles seen many giant planets <sup>87-90</sup>.

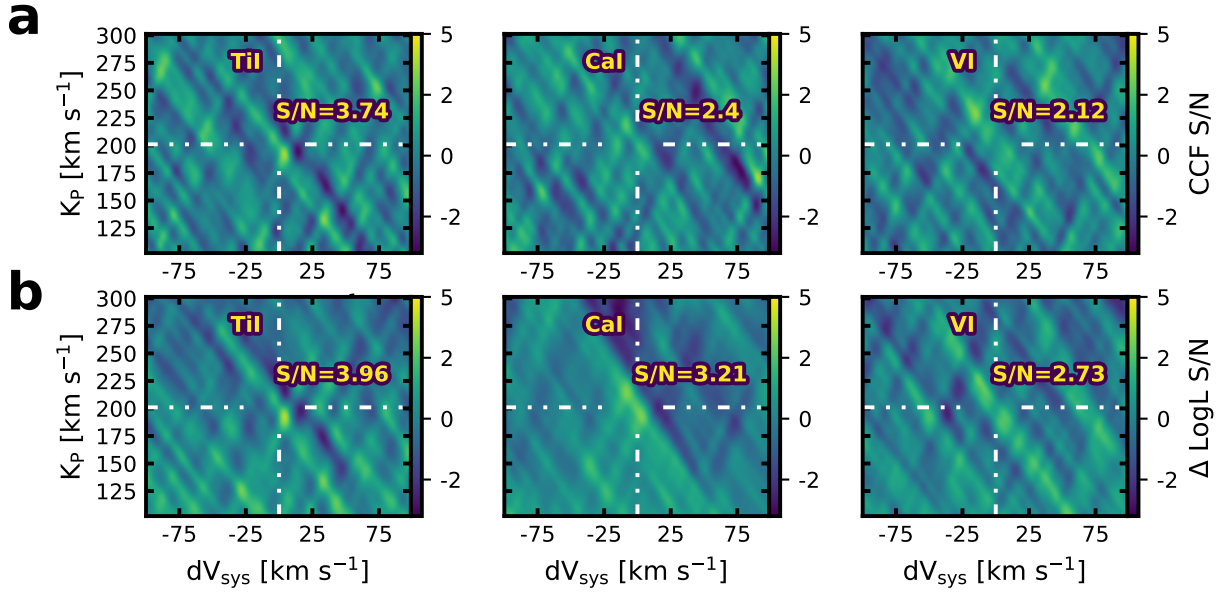
Ultimately, determining the exact location of the formation for hot Jupiters remain a non-trivial task, as migration through different disk regions and the evolution of the disk through time are factors that would also need to be considered. More modeling would be required to con-

sider these factors when attempting to reconstruct the formation history of such a unique system, and underscores the difficulty of using present-day gas abundance measurements to estimate the formation pathways of giant planets. To more rigorously address planet formation trends, such measurements over a larger sample of planets is needed.

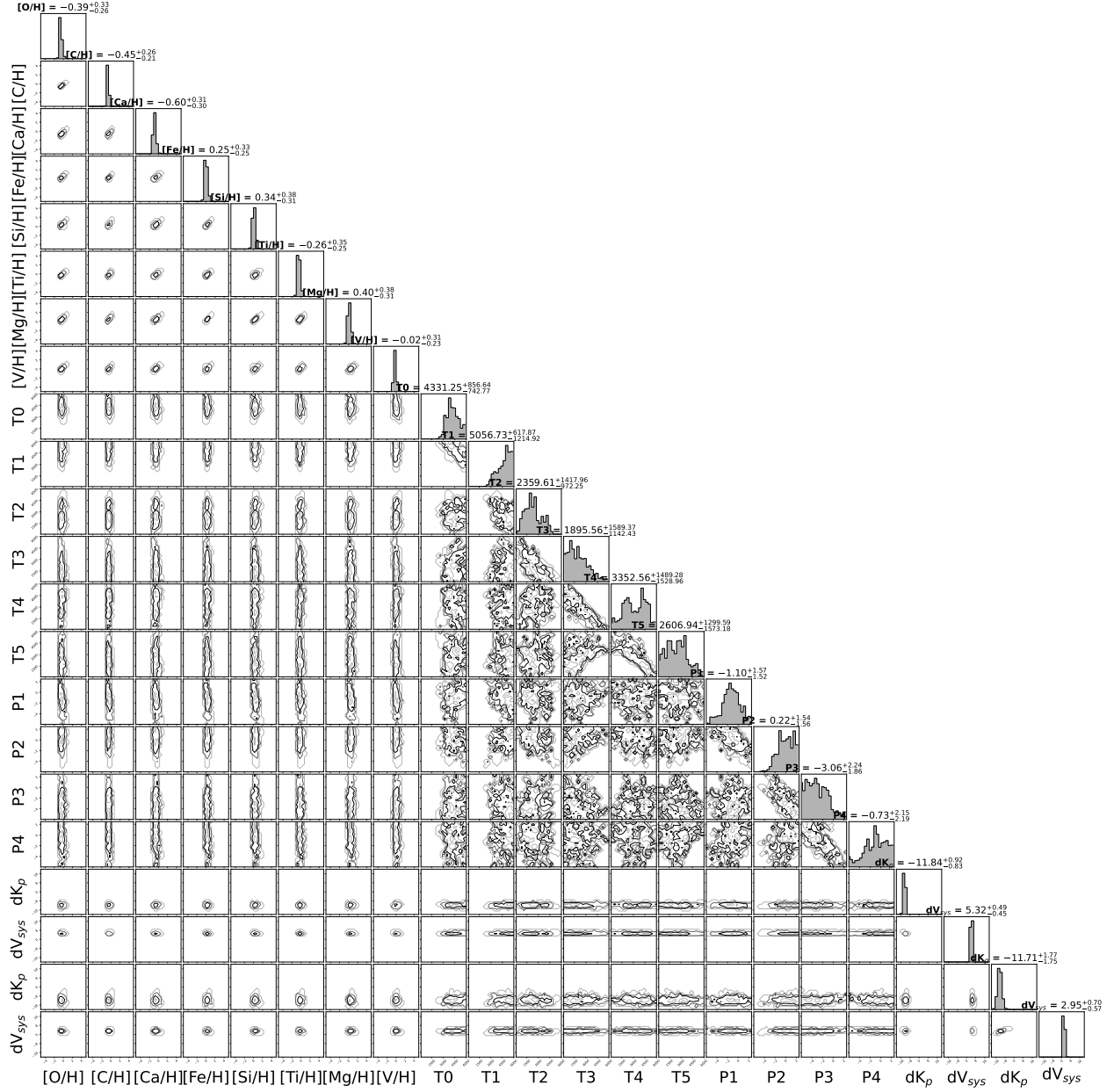
## Supplementary Figures



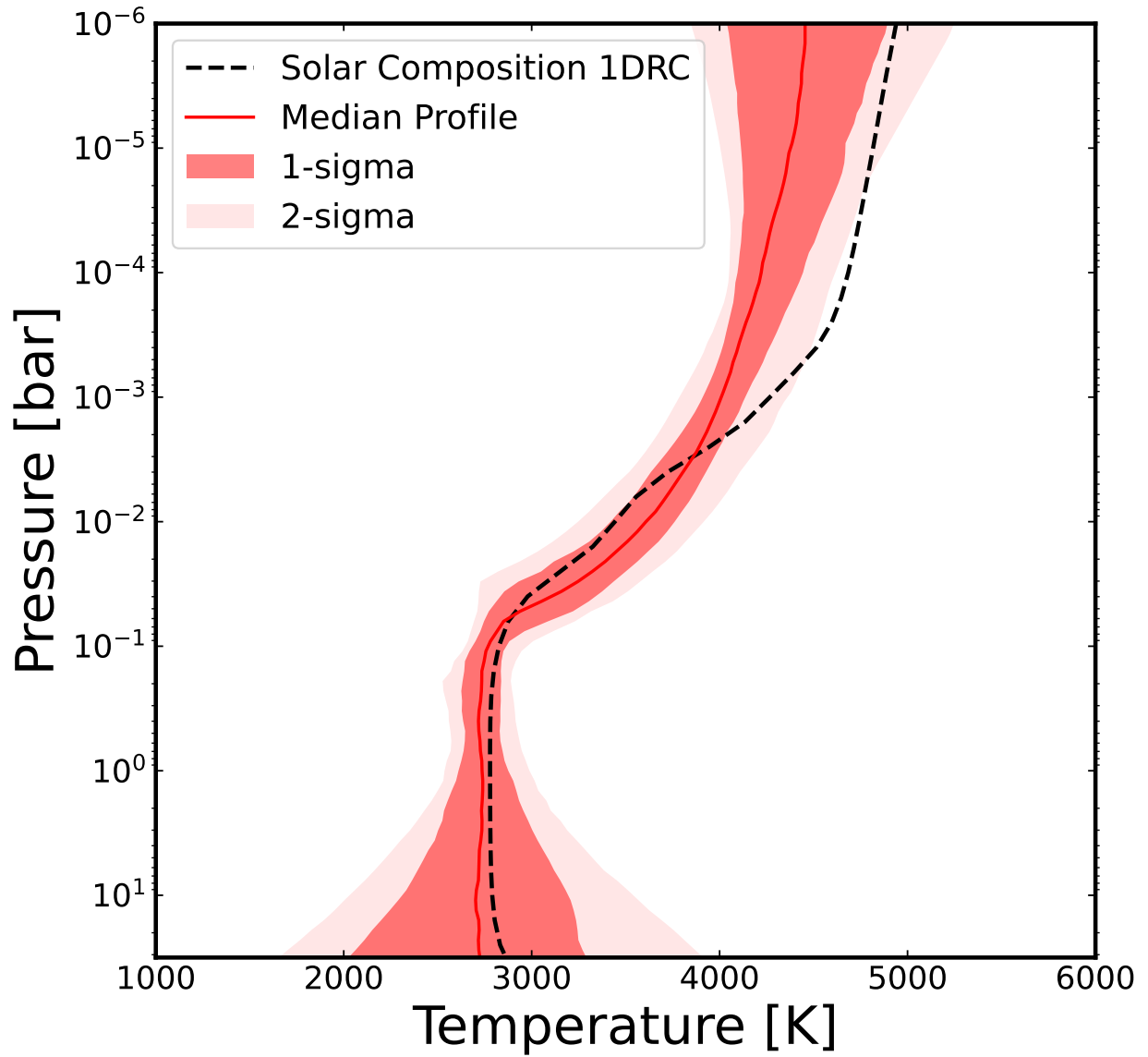
Supplementary Figure 1: **Observing conditions during each night.** **a** Median observed SNR during each frame of the pre (blue) and post (red) eclipse sequences. **b** Humidity during the observations for the pre (blue) and post (red) eclipse observations. Each frame refers to an AB pair in the AB-BA nodding pattern during observations. In total there were 155 frames for the pre eclipse sequence and 84 for the post eclipse sequence.



Supplementary Figure 2: **Summary of weak-to-non detections using the individual gas templates of Ti I, Ca I and V I.** **a** Cross correlation S/N maps for individual gas templates of Ti I, Ca I and V I. **b** These same S/N detection maps, but instead calculated using the log-likelihood formalism as described in ref <sup>21</sup>.

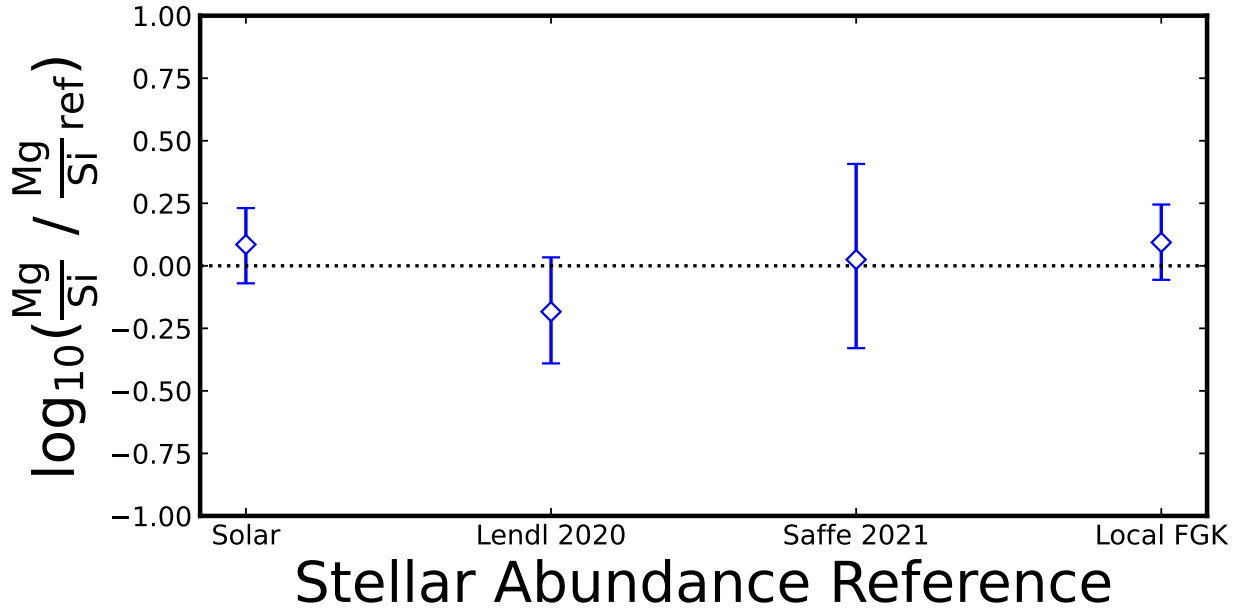


Supplementary Figure 3: **Full corner plot of the posterior probability distribution from the retrieval in our main result.** The first 8 parameters are the enrichment in the gas abundance, relative to solar, for each species in our model. The next 10 are TP profile parameters. Finally, the last 4 are the  $dK_P$  and  $dV_{sys}$  pair for each night. The total number of parameters is 22.

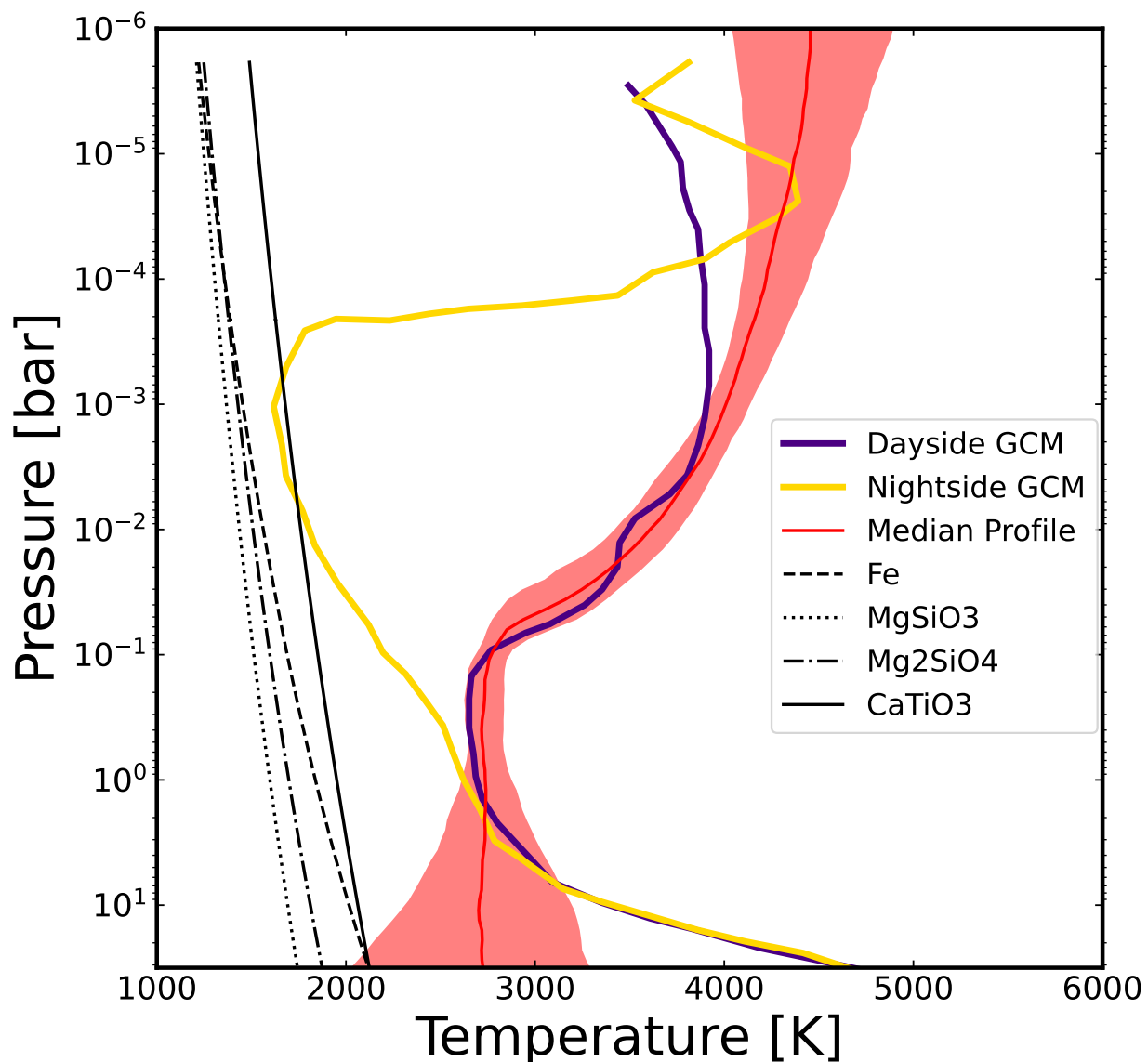


Supplementary Figure 4: **Pressure-Temperature profile for WASP-189b from our main retrieval result.** The median profile (red line) along with the 1 and  $2\sigma$  confidence intervals around this median are shown, generated via 1000 random draws from the posterior distribution. We also show another P-T profile for WASP-189b generated under radiative-convective-thermochemical equilibrium conditions. Source data are provided as a Source Data file.

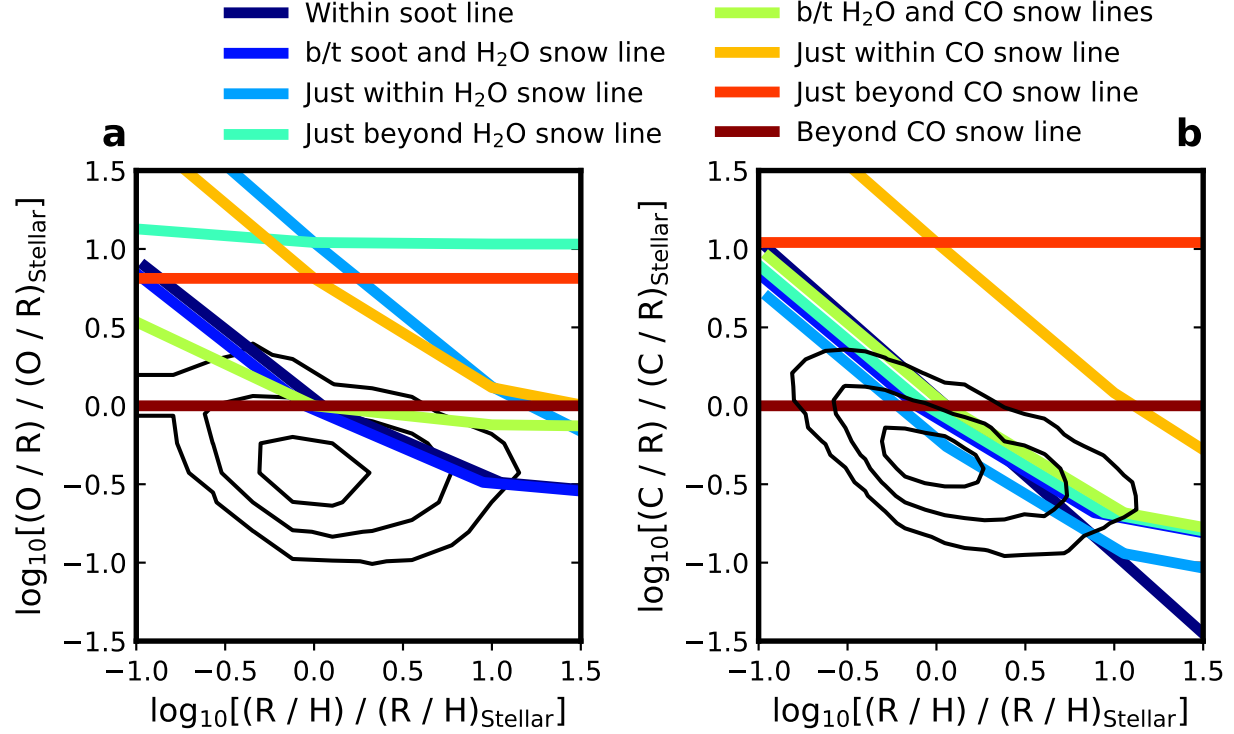




Supplementary Figure 5: **Logarithm of the Magnesium to Silicon (Mg/Si) ratio calculated in this analysis for the planet WASP-189b with respect to different astrophysical measurements of the ratio of Mg/Si.** The first tick shows the  $\log_{10}$  ratio of Mg/Si in WASP-189b, measured in this work, over the Solar ratio of Mg/Si from ref <sup>36</sup>. The second and third ticks compute the  $\log_{10}$  ratio of Mg/Si in the WASP-189b to two different references to the Mg/Si ratio of the host star WASP-189; tick mark Lendl 2020 is from ref <sup>18</sup>, the main set of stellar abundances used in this analysis, and tick mark Saffe 2021 uses the computed Mg/Si ratio per the stellar abundances as reported in ref <sup>79</sup>. Finally, the tick Local FGK uses measured value in the local FGK population as cited in <sup>40</sup>. All errorbars represent the 68 % confidence interval on each measurement. Source data are provided as a Source Data file.



Supplementary Figure 6: **Thermal structure of WASP-189b with the  $1\sigma$  confidence interval (red) as compared to condensation curves for Fe, Si, Ca and Ti bearing species (black lines).** In yellow and indigo we show the vertical P-T profiles for the day-and-night sides for WASP-189b as predicted by the Global Circulation Models from <sup>85</sup>. Our retrieved thermal structure shows good agreement with the predictions for the day-side hemisphere of this ultra-hot Jupiter. Moreover, because our retrieved P-T profile does not cross the condensation curves of for these condensates, we do not expect the depletion of these species due to their condensation to bias our final results. Source data are provided as a Source Data file.



Supplementary Figure 7: **Predicted formation scenarios for WASP-189b based on our retrieved abundances.** **a** Oxygen to refractory abundance ratio in WASP-189b as a function of the total refractory content, relative to the stellar values calculated from <sup>18</sup>. **b** Same as **a** but with the carbon abundance instead of oxygen. The colored lines represent different formation predictions described in the modeling framework from <sup>11</sup>. The legend above indicates the predicted formation location within the disk that would produce the final observed combination of  $[R/H]_*$  and  $[O/R]_*$  or  $[C/R]_*$ . Our measured  $[R/H]_*$ ,  $C/O$  and  $[R/V]_*$  ratios are consistent with formation interior to the snow lines, with an accretion history of a stellar proportion of solids to gas, with those solids being slightly more rich in refractory to volatiles. However, the uncertainties on our  $[R/V]_*$  measurement means we cannot rule out formation beyond the CO snow line. This ambiguity highlights the difficulty in predicting exact formation locations within the protoplanetary disk for hot Jupiters <sup>14,91</sup>. The 2D histogram show the 39.3, 86.4 and 98.9% joint probability contours for these quantities.

## Supplementary Tables

Element	$\log(X/H)$	$[X/H]_{\odot}$	$[X/H]_{*L20}$	$[X/H]_{*S21}$	$[X/H]_{*La24}$
O	$-3.69^{+0.33}_{-0.26}$	$-0.38^{+0.33}_{-0.25}$	$-0.38^{+0.36}_{-0.27}$	—	—
C	$-3.99^{+0.26}_{-0.21}$	$-0.45^{+0.26}_{-0.21}$	$-0.31^{+0.29}_{-0.23}$	$-0.02^{+0.33}_{-0.27}$	—
Ca	$-6.30^{+0.31}_{-0.30}$	$-0.60^{+0.31}_{-0.30}$	$-0.85^{+0.29}_{-0.23}$	$-0.67^{+0.46}_{-0.45}$	$-1.08^{+0.32}_{-0.32}$
Fe	$-4.28^{+0.33}_{-0.25}$	$0.25^{+0.33}_{-0.25}$	$-0.08^{+0.35}_{-0.29}$	$0.22^{+0.36}_{-0.30}$	$-0.29^{+0.35}_{-0.28}$
Si	$-4.14^{+0.38}_{-0.31}$	$0.34^{+0.38}_{-0.31}$	$0.20^{+0.38}_{-0.31}$	$0.27^{+0.41}_{-0.38}$	—
Ti	$-7.29^{+0.35}_{-0.25}$	$-0.26^{+0.35}_{-0.25}$	$-0.02^{+0.38}_{-0.25}$	$-0.29^{+0.36}_{-0.28}$	$-0.56^{+0.35}_{-0.27}$
Mg	$-4.05^{+0.37}_{-0.30}$	$0.39^{+0.37}_{-0.30}$	$-0.01^{+0.39}_{-0.33}$	$0.29^{+0.44}_{-0.39}$	$-0.30^{+0.31}_{-0.30}$
V	$-8.12^{+0.31}_{-0.23}$	$-0.02^{+0.31}_{-0.23}$	—	—	—

Supplementary Table 1: **Retrieved abundance pattern measured in the atmosphere of WASP-189b.** The first column shows each elemental species in our model. Column 2 has the abundance ratio of  $\log(X/H)$  for each element, X, measured in the atmosphere of WASP-189b. Columns 3, 4, 5 and 6 show these ratios as compared to both solar and various literature stellar values. Column 3 is the  $\log(X/H)$  relative to the solar value <sup>36</sup> (the main output of the retrieval). (To calculate column 2 from column 3, we add each value of column 3 with the  $\log_{10}(\frac{X}{H})$  solar value as reported in <sup>36</sup>). Column 4 are these ratios relative to the stellar values of ref <sup>18</sup> (L20). Column 5 are ratios relative to the values reported in ref <sup>79</sup> (S21) and column 6 the values from ref <sup>80</sup> (La24). When the abundance of a species is not reported, it is not listed. For all stellar species with reported uncertainties, the shown uncertainties reflect the 68% confidence interval.